# Effect of surface acidity modulation on Pt/Al<sub>2</sub>O<sub>3</sub> single atom catalyst for 1 carbon monoxide oxidation and methanol decomposition 2 Shaohua Xie, a Xing Zhanga, Peng Xu, b Braden Hatcher, c Yuxi Liu, d Lu Ma, e Steven N. 3 Ehrlich, e Sampyo Hong, c Fudong Liu\*, a 4 5 <sup>a</sup> Department of Civil, Environmental, and Construction Engineering, Catalysis Cluster for 6 Renewable Energy and Chemical Transformations (REACT), NanoScience Technology 7 Center (NSTC), University of Central Florida, Orlando, FL 32816, United States 8 <sup>b</sup> CAS Key Laboratory of Standardization and Measurement for Nanotechnology, National 9 Center for Nanoscience and Technology, Beijing 100190, China <sup>c</sup> Brewton-Parker College, Mount Vernon, GA 30445, United States 10 <sup>d</sup> College of Environmental and Energy Engineering, Beijing University of Technology, 11 12 Beijing 100124, China 13 <sup>e</sup> National Synchrotron Light Source II (NSLS-II), Brookhaven National Laboratory, Upton, 14 NY 11973, United States 15 \* Corresponding author. Email address: fudong.liu@ucf.edu (F. Liu) 16

#### Abstract

17

18

19

20

21

22

23

24

25

26

27

28

29

30

31

32

33

34

35

36

37

38

With ideal metal utilization efficiency and homogeneous active sites, single atom catalysts (SACs) have attracted extensive attention in heterogeneous catalysis field. The performance of SACs is highly dependent on the local coordination environment of metal single atoms. However, few works reported the effect of surface acidity modification on the performance of SACs such as Pt SACs which have been widely studied nowadays. In this work, a Pt/Al<sub>2</sub>O<sub>3</sub> SAC has been successfully prepared using a bayerite Al(OH)<sub>3</sub> as support through simple IWI method for Pt loading. Through post-modification of Pt/Al<sub>2</sub>O<sub>3</sub> with acidic WO<sub>3</sub> and basic MgO, the surface acidity of Pt/Al<sub>2</sub>O<sub>3</sub> was tuned. Activity of CO oxidation and methanol decomposition on the modified catalysts has been evaluated. It was found that the catalytic performance was highly related to the surface acidity of Pt SACs. Basic MgO modified Pt/Al<sub>2</sub>O<sub>3</sub> performed better in CO oxidation under the reaction condition with H<sub>2</sub>O. Acidic WO<sub>3</sub> modified Pt/Al<sub>2</sub>O<sub>3</sub> showed superior activity in methanol decomposition. Detailed characterization and in situ diffuse reflectance infrared Fourier transform spectroscopy (DRIFTS) study suggested that the positive H<sub>2</sub>O effect on CO oxidation was due to the mitigated formation of bicarbonate species on Pt/Al<sub>2</sub>O<sub>3</sub> and WO<sub>3</sub>/Pt/Al<sub>2</sub>O<sub>3</sub> catalysts and the promoted desorption of carbonate species from MgO/Pt/Al<sub>2</sub>O<sub>3</sub>. The superior methanol decomposition performance on WO<sub>3</sub>/Pt/Al<sub>2</sub>O<sub>3</sub> was owing to its abundant oxygen vacancies and high resistance to carbonate accumulation. This study highlights the importance of surface acidity modulation of Pt SACs in heterogeneous catalysis and suggests that fine-tuning the surface acidity can be an effective strategy in new SACs development.

### Keywords

- 39 Platinum single atom catalyst; acidity modification; carbon monoxide oxidation; methanol
- 40 decomposition; carbonate resistance

#### 1. Introduction

42

66

43 As a rising star in material science, supported single atom catalysts (SACs) in which metal species are atomically dispersed on solid supports, have attracted extensive attention in various 44 45 applications including biocatalysis, photocatalysis, electrocatalysis and thermal-catalysis [1]. 46 Due to its relatively homogeneous active sites, SACs not only can show great benefits on 47 improving catalytic activity but also can enhance selectivity in specific reactions. In addition, 48 with maximum atomic utilization efficiency, SACs can contribute to more sustainable 49 utilization of platinum group metals (PGMs), which are expensive, critical and difficult to have 50 alternatives in multiple catalysis reactions [2, 3]. 51 To increase the metal utilization efficiency and activity of supported Pt catalysts, Pt SAC on 52 diverse supports have been developed and applied in many reactions, including hydrogenation 53 [4], dehydrogenation [5], volatile organic compounds combustion [6, 7], the water-gas shift [8], 54 CO oxidation [9], and alcohol decomposition [10]. For instance, Pt SACs on reducible metal 55 oxide supports such as CeO<sub>2</sub>, FeO<sub>x</sub> and MnO<sub>x</sub>, or their derived catalysts showed superior 56 catalytic performance for the hydrogenation of 3-nitrostyrene [11], CO oxidation [12-15]. hydrocarbon oxidation [11, 16, 17], H<sub>2</sub> production from methanol decomposition [10, 18] and 57 58 hydrocarbon reforming [19]. Pt SACs on irreducible metal oxide supports including ZrO<sub>2</sub> and 59 Al<sub>2</sub>O<sub>3</sub> also have been fabricated for various applications [20-22]. Zhang et al. reported that Pt 60 single atom catalyst on mesoporous Al<sub>2</sub>O<sub>3</sub> showed excellent performance and stability for n-61 hexane hydro-reforming, high activity for the selective hydrogenation of 1,3-butadiene, and superior stability in CO oxidation [21]. Liu et al. developed a methodology of electron-62 microscopy-based atom recognition statistics (EMARS) for determining the density of Pt single 63 64 atoms on Al<sub>2</sub>O<sub>3</sub>, and then concluded that the activity for aromatics production from 65 hydrocarbon reforming quantitatively correlated with the density of Pt single-atoms [22].

A challenge in the development of efficient SACs is the modulation of metal local

coordination environment, which has been verified governing the catalytic performance in certain catalysis reactions [23-25]. Xu et al. claimed that propylene selectivity was highly related to the coordination number of Pt-O in Pt/CeO<sub>2</sub> for propyne semihydrogenation reaction [25]. With high-entropy oxides (HEOs) modification on Al<sub>2</sub>O<sub>3</sub>, Zhao et al. found that Pt-HEO/Al<sub>2</sub>O<sub>3</sub> SAC exhibited superior stability against hydrothermal aging and long-term catalytic stability for CO oxidation comparing to the conventional Pt SACs [26]. Wang et al. reported a promotion effect of barium modification on hydrothermal stability of Pt/La-Al<sub>2</sub>O<sub>3</sub> SAC for CO and C<sub>3</sub>H<sub>6</sub> oxidation [27]. However, so far, there have been no known reports on studying the effects of surface acidity modification of Pt/Al<sub>2</sub>O<sub>3</sub> SACs for CO oxidation and methanol decomposition. Therefore, in this work, through post-modification on Pt/Al<sub>2</sub>O<sub>3</sub> SAC with acidic WO<sub>3</sub> and basic MgO, Pt/Al<sub>2</sub>O<sub>3</sub> SACs with different surface acidity have been fabricated and applied in CO oxidation and methanol decomposition. By means of in situ diffuse reflectance infrared Fourier transform spectroscopy (DRIFTS) of CO adsorption at room temperature, High-angle annular dark-field scanning transmission electron microscopy (HAADF-STEM) and energy dispersive x-ray spectroscopy (EDS) mapping, as well as extended X-ray absorption fine structure (EXAFS) of Pt L<sub>III</sub>-edge, Pt single atom structure in the fabricated catalysts has been confirmed. Catalytic behaviors on Pt/Al<sub>2</sub>O<sub>3</sub> SACs with different surface acidity property for CO oxidation and methanol decomposition have been investigated in detail. It was proposed that the CO oxidation and methanol decomposition performance was highly associated with the surface acidity of Pt SACs catalysts. Through systematic in situ DRIFTS study, the structure-activity relationship for both CO oxidation and methanol decomposition on different catalysts has also been discussed.

# 2. Experimental section

### 90 **2.1. Materials**

67

68

69

70

71

72

73

74

75

76

77

78

79

80

81

82

83

84

85

86

87

88

89

91 Commercial non-dispersible bayerite Al(OH)<sub>3</sub> support with a particle size of ca. 5-10 µm and

BET surface area of *ca*. 360 m<sup>2</sup>/g was obtained from Sasol. Platinum (IV) nitrate was purchased from Umicore Precious Metals Chemistry, LLC. Ammonium metatungstate hydrate (99.5%), magnesium nitrate (99.5%) and methanol (99.8%) were purchased from Alfa Aesar. 10% H<sub>2</sub>/Ar, 10% CO/Ar, N<sub>2</sub> (99.999%), O<sub>2</sub> (99.999%) and Ar (99.999%) gas cylinders were purchased from Airgas. No further treatment was conducted on all chemicals and cylinders used in this

### 2.2. Catalyst preparation

work.

An incipient wetness impregnation (IWI) method was adopted for the preparation of all samples. For Pt/Al<sub>2</sub>O<sub>3</sub> catalyst, platinum (IV) nitrate solution with 1 wt.% Pt was added dropwise onto Al(OH)<sub>3</sub> support and then dried at 120 °C for 1 h. Followed by calcination at 550 °C for 2 h in air with a temperature ramp of 5 °C/min, the 1 wt.% Pt/Al<sub>2</sub>O<sub>3</sub> catalyst was prepared. The WO<sub>3</sub>/Pt/Al<sub>2</sub>O<sub>3</sub> and MgO/Pt/Al<sub>2</sub>O<sub>3</sub> catalysts were obtained by dropwise adding ammonium metatungstate or magnesium nitrate solution (5 wt.% WO<sub>3</sub> or 5 wt.% MgO) onto Pt/Al<sub>2</sub>O<sub>3</sub>, followed by calcination at 550 °C for 2 h in air with a temperature ramp of 5 °C/min. The pure Al<sub>2</sub>O<sub>3</sub> support was prepared by calcining Al(OH)<sub>3</sub> at 550 °C for 2 h, and WO<sub>3</sub>/Al<sub>2</sub>O<sub>3</sub> and MgO/Al<sub>2</sub>O<sub>3</sub> reference samples were also prepared by skipping the Pt impregnation step.

### 2.3. Catalyst characterizations

X-ray powder diffraction (XRD) testing was performed on a PANalytical Empyrean diffractometer using a Cu K $\alpha$  X-rays ( $\lambda$  = 0.15406 nm). The collection range of XRD patterns was 10-80 °, and the scan speed was 6 °/min with a scan step of 0.067 °.

Nitrogen (N<sub>2</sub>) adsorption-desorption isotherm analysis was performed on a Quantachrome Autosorb-iQ instrument with the samples degassed at 300 °C for 2 h under vacuum before measurement. Brunauer-Emmett-Teller (BET) surface areas were calculated using adsorption points in the relative pressures between 0.05 and 0.3. The pore size distribution was determined by non-local density functional theory (DFT) method.

117 High-angle annular dark-field scanning transmission electron microscopy (HAADF-STEM) 118 and energy dispersive x-ray spectroscopy (EDS) mapping were performed on a JEOL-2100F 119 equipment. 120 To determine the binding energies (BEs) of Al 2p, W 4f, Mg 2p, O 1s, Pt 4d, and C 1s for all the samples, X-ray photoelectron spectroscopy (XPS) analysis was conducted on a VG 121 CLAM 4 MCD analyzer using Mg K- $\alpha$  (hv = 1253.6 eV) as an excitation source. All samples 122 were degassed in the preparation chamber (10<sup>-5</sup> Torr) for 0.5 h and then introduced into the 123 analysis chamber (3  $\times$  10<sup>-9</sup> Torr) for XPS collection. The BE calibration was conducted using 124 125 C 1s signal at 284.6 eV as reference. X-ray absorption near edge structure (XANES) and extended X-ray absorption fine structure 126 127 (EXAFS) of Pt L<sub>III</sub>-edge and W L<sub>III</sub>-edge were measured in fluorescent mode for all catalysts 128 and in transmission mode for all foils or oxide references at room temperature at 7-BM QAS 129 beamline of the National Synchrotron Light Source II (NSLS-II), Brookhaven National 130 Laboratory. Data was analyzed using Athena and Artemis software from the Demeter package. 131 Pt and W foil were applied for energy calibration and drift correction of the monochromator. The processed EXAFS,  $\chi(k)$ , was weighted by  $k^2$  for Pt L<sub>III</sub>-edge and  $k^3$  for W L<sub>III</sub>-edge to 132 133 amplify the high-k oscillations. For Fourier-transformed (FT) spectra, the k ranges between 3.0 to 11.0 Å<sup>-1</sup> for Pt L<sub>III</sub>-edge and 2.0 to 12.0 Å<sup>-1</sup> for W L<sub>III</sub>-edge were used, and the fitting in the 134 R ranges for all catalysts were between 1.0 to 3.0 Å for Pt L<sub>III</sub>-edge and 1.0 to 2.0 Å for W L<sub>III</sub>-135 136 edge in Artemis software. 137 H<sub>2</sub> temperature-programmed reduction (H<sub>2</sub>-TPR) was performed on a Quantachrome Autosorb-iQ instrument. Prior to test, 30 mg of the catalyst was treated in a flow of 5 vol.% 138 O<sub>2</sub>/He (40 sccm) at 300 °C for 1 h to remove the possible surface adsorbents and then cooled 139 140 down to 30 °C. Afterwards, the temperature was increased from 40 to 500 °C linearly with a ramping rate of 10 °C/min in a flow of 10 vol.% H<sub>2</sub>/Ar (30 sccm). A thermal conductivity 141

detector (TCD) was used to monitor the signal of H<sub>2</sub> consumption. Calculation of H<sub>2</sub> consumption was performed using CuO as a reference.

142

143

144

145

146

147

148

149

150

151

152

153

154

155

156

157

158

159

160

161

162

163

164

165

166

Pt dispersion of the samples were determined by a CO pulse titration experiment performed on Quantachrome Autosorb-iQ instrument as well. Typically, 50 mg sample was loaded into a U-shaped quartz reactor with an inner diameter of 8 mm. Afterwards, in order to obtain pure metallic Pt sites for CO adsorption, a typical pretreatment in 10% H<sub>2</sub>/Ar flow at 400 °C for 1 h was conducted, followed by He purge at 400 °C for 30 min (avoiding the presence of residual adsorbed hydrogen) and cooling down to 25 °C. Afterwards, He was used as carried gas at 50 sccm, and successive doses of CO gas were introduced into the He stream by a calibrated injection valve (150 µL 5% CO/He per pulse) at 25 °C. The titration was considered as finished when the intensities of three peaks in a row kept constant. In situ diffuse reflectance infrared Fourier transform spectroscopy (in situ DRIFTS) experiments were carried out on Nicolet iS50 FT-IR spectrometer with a liquid nitrogencooling MCT detector. Prior to in situ DRIFTS experiment, 20 mg sample was loaded into a high temperature IR cell (PIKE DiffusIR cell with ZnSe windows), followed with a treatment in 10% O<sub>2</sub>/Ar flow (30 sccm) at 300 °C for 1 h. Subsequently, the sample was cooled to target temperature (25, 50, 100, 150, 200, 250, 300, or 350 °C) followed by Ar purge (50 sccm) for 30 min before collecting the background spectrum. The infrared spectra were collected by accumulating 100 scans at a spectral resolution of 4 cm<sup>-1</sup>. For CO adsorption at 25 °C, 1% CO balanced with Ar was introduced into the cell for 30 min to achieve saturated CO adsorption on sample. Then, the flow of CO was discontinued, and the sample was exposed to Ar flow for 15 min to remove weakly adsorbed CO. For CO oxidation at 200 °C with/without water, 1% CO, 1% O<sub>2</sub> and 5% H<sub>2</sub>O (when used) balanced with Ar were introduced into the cell for 60

min to achieve a steady-state CO oxidation on sample. Afterwards, the flow of CO was

discontinued, and the sample was exposed to 1% O2 and 5% H2O (when used) balanced with

Ar for 30 min to react with surface adsorbed CO. For NH<sub>3</sub> adsorption/desorption experiments, the NH<sub>3</sub> adsorption was performed on the sample at 50 °C in the flow of 500 ppm NH<sub>3</sub> for 1 h. Then, the sample was purged by Ar for 30 min until the IR signals were stabilized. Afterwards, the desorption experiments were carried out in Ar flow with the temperature increased from 50 to 350 °C, respectively. For methanol decomposition at 240 °C, a flow of 10% CH<sub>3</sub>OH balanced with Ar was introduced into the cell for 30 min until the IR signals were stabilized. Then, methanol desorption was carried out in Ar flow at 240 °C for 30 min after methanol was discontinued. The DRIFTS spectra were recorded during the whole methanol decomposition and desorption process.

### 2.4. Catalytic performance evaluation

Catalytic activity evaluation for CO oxidation and CH<sub>3</sub>OH decomposition over all catalysts was carried out on a continuous flow fixed-bed quartz tubular microreactor (internal diameter = 4.0 mm). For CO oxidation, 25 mg of the catalyst (40-60 mesh) was diluted with 0.25 g of inert SiC (40-60 mesh) to minimize the effect of hot spots. The reactant mixture was composed of 1% CO, 1% O<sub>2</sub> and 5% H<sub>2</sub>O (when used) (Ar balance), and the total flow was 83.33 sccm, thus giving a WHSV of 200,000 mL g<sup>-1</sup> h<sup>-1</sup>. In the case of water vapor introduction, 5% H<sub>2</sub>O was introduced by passing a carrier gas (Ar) through a water saturator at 60 °C. For CH<sub>3</sub>OH decomposition, a flow of 10% CH<sub>3</sub>OH balanced with Ar of 83.33 sccm obtained by passing a carrier gas (Ar) through a CH<sub>3</sub>OH saturator at 35 °C was used, thus giving a WHSV of 50,000 mL g<sup>-1</sup> h<sup>-1</sup>. Reactants and products were analyzed online by a Mass Spectrometer (MS, Hiden Analytical). The m/z ratios used for CO, O<sub>2</sub>, CO<sub>2</sub>, H<sub>2</sub> and CH<sub>3</sub>OH detection were 28, 32, 44, 2 and 31, respectively. The reactant conversion was defined as ( $c_{inlet}$  -  $c_{outlet}$ )/ $c_{inlet}$  × 100%, where  $c_{inlet}$  and  $c_{outlet}$  were the inlet and outlet CO/CH<sub>3</sub>OH concentrations in the feed stream, respectively.

#### 3. Results and discussion

### 3.1. Catalyst structure characterization

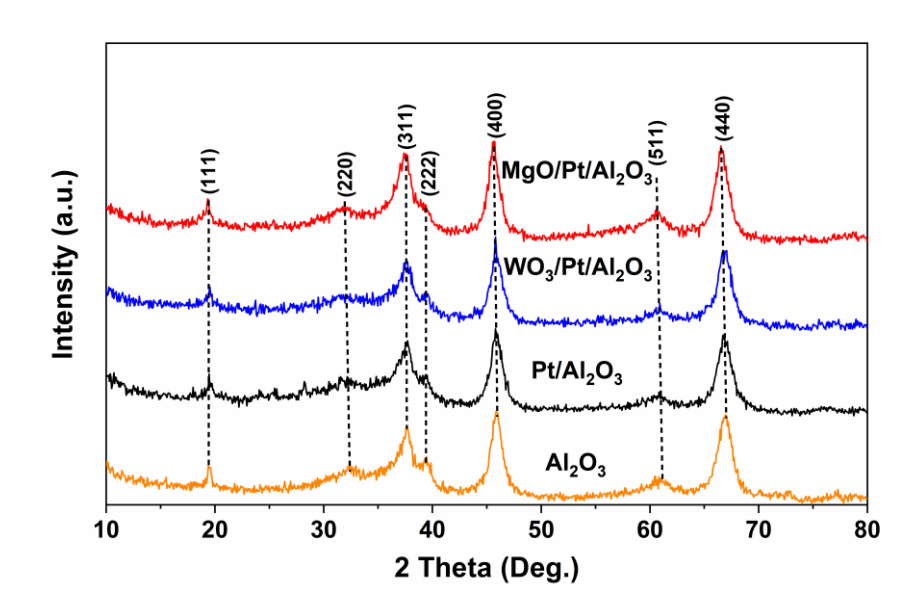


Fig. 1. XRD patterns of Al<sub>2</sub>O<sub>3</sub> support, Pt/Al<sub>2</sub>O<sub>3</sub>, WO<sub>3</sub>/Pt/Al<sub>2</sub>O<sub>3</sub> and MgO/Pt/Al<sub>2</sub>O<sub>3</sub> catalysts.

**Fig. 1** shows the XRD patterns of pristine Al<sub>2</sub>O<sub>3</sub> support, Pt/Al<sub>2</sub>O<sub>3</sub>, WO<sub>3</sub>/Pt/Al<sub>2</sub>O<sub>3</sub> and MgO/Pt/Al<sub>2</sub>O<sub>3</sub> catalysts. For the Al<sub>2</sub>O<sub>3</sub> support obtained from pre-calcination of bayerite Al(OH)<sub>3</sub> at 550 °C, the formed Al<sub>2</sub>O<sub>3</sub> showed an  $\eta$ -Al<sub>2</sub>O<sub>3</sub> phase according to the Inorganic Crystal Structure Database (ICSD code 66558) [28]. It was reported that  $\eta$ -Al<sub>2</sub>O<sub>3</sub> has very similar bulk structure to  $\gamma$ -Al<sub>2</sub>O<sub>3</sub>, but due to the difference in surface Al coordination,  $\eta$ -Al<sub>2</sub>O<sub>3</sub> has greater Lewis acidity than  $\gamma$ -Al<sub>2</sub>O<sub>3</sub> [29]. Greater Lewis acidity and possibly more surface defects on  $\eta$ -Al<sub>2</sub>O<sub>3</sub> should be beneficial in highly dispersing the loaded components comparing to that on the conventional  $\gamma$ -Al<sub>2</sub>O<sub>3</sub>. For the Pt/Al<sub>2</sub>O<sub>3</sub> catalyst, no peaks indexed to Pt metal or Pt oxides were found from its XRD pattern, suggesting that the Pt species was highly dispersed on Al<sub>2</sub>O<sub>3</sub> surface. It has to be noted that the diffraction peaks of  $\eta$ -Al<sub>2</sub>O<sub>3</sub> in Pt/Al<sub>2</sub>O<sub>3</sub> catalyst showed weaker intensity and broader full width at half maximum (FWHM). This indicates that the impregnation of Pt nitrate onto bayerite Al(OH)<sub>3</sub> followed by calcination actually hindered the growth of resulting Al<sub>2</sub>O<sub>3</sub> crystallites to a certain extent (comparing to the pristine  $\eta$ -Al<sub>2</sub>O<sub>3</sub>) probably due to the strong interaction between highly dispersed Pt species and  $\eta$ -Al<sub>2</sub>O<sub>3</sub>. This conclusion can be further confirmed by the calculated Al<sub>2</sub>O<sub>3</sub> crystallite sizes according to

Scherrer equation using the FWHM of Al<sub>2</sub>O<sub>3</sub> (400) peak, as shown in **Table 1**. The post-impregnation of acidic WO<sub>3</sub> and basic MgO onto Pt/Al<sub>2</sub>O<sub>3</sub> catalyst did not obviously influence the Al<sub>2</sub>O<sub>3</sub> crystal structure. The absence of typical diffraction peaks of WO<sub>3</sub> and MgO suggested that the W and Mg species were also highly dispersed without long-range order within WO<sub>3</sub>/Pt/Al<sub>2</sub>O<sub>3</sub> and MgO/Pt/Al<sub>2</sub>O<sub>3</sub> catalysts, respectively.

Table 1. BET surface area,  $Al_2O_3$  crystallite size ( $D_{Al_2O_3}$ ), average pore size, and pore volume of different samples.

Sample	BET surface area <sup>a</sup> (m <sup>2</sup> /g)	<i>D</i> <sub>Al<sub>2</sub>O<sub>3</sub><sup>b</sup> (nm)</sub>	Average pore size <sup>c</sup> (nm)	Pore volume (cm <sup>3</sup> /g)	Pt dispersion <sup>d</sup> (%)
Al <sub>2</sub> O <sub>3</sub>	273	6.4	3.2	0.33	-
$Pt/Al_2O_3$	238	5.5	3.6	0.29	54.0
$WO_3/Pt/Al_2O_3$	240	6.0	3.5	0.29	52.5
$MgO/Pt/Al_2O_3$	202	6.1	3.8	0.26	30.1

<sup>&</sup>lt;sup>a</sup> Obtained using the BET method;

210

211

212

213

<sup>218</sup> b Estimated according to the Scherrer equation using the full width at half maximum (FWHM)

<sup>219</sup> of Al<sub>2</sub>O<sub>3</sub> (400) peak;

<sup>&</sup>lt;sup>c</sup> Estimated according to the DFT method;

d Obtained by CO pulse titration experiment for samples after pre-reduction by H<sub>2</sub> at 400 °C

<sup>222</sup> for 1 h.

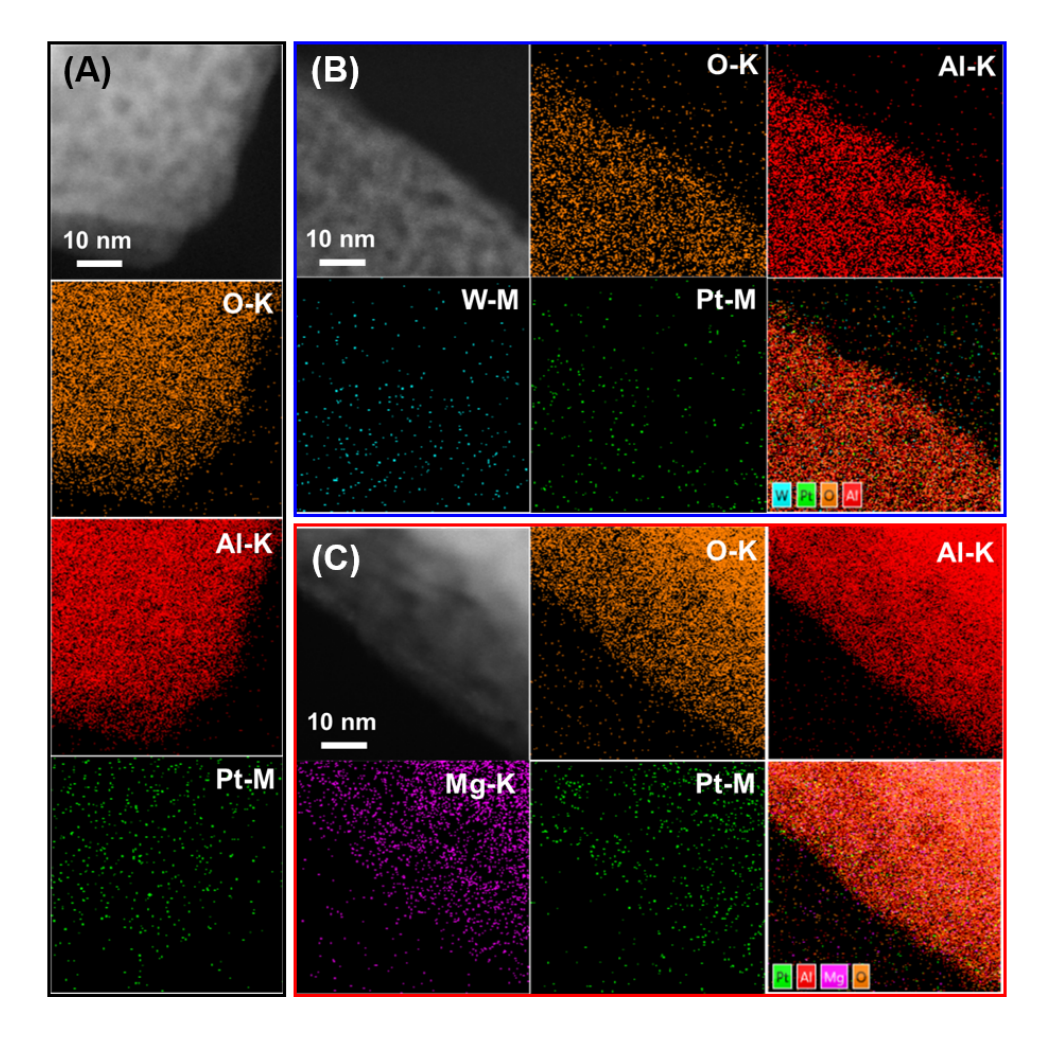


**Fig. 2.** HAADF-STEM and EDS mapping results for (A) Pt/Al<sub>2</sub>O<sub>3</sub>, (B) WO<sub>3</sub>/Pt/Al<sub>2</sub>O<sub>3</sub> and (C) MgO/Pt/Al<sub>2</sub>O<sub>3</sub>.

Fig. S1 (see Supplementary Material) shows the N<sub>2</sub> adsorption/desorption isotherms and pore size distribution of Al<sub>2</sub>O<sub>3</sub>, Pt/Al<sub>2</sub>O<sub>3</sub>, WO<sub>3</sub>/Pt/Al<sub>2</sub>O<sub>3</sub> and MgO/Pt/Al<sub>2</sub>O<sub>3</sub> samples. All the N<sub>2</sub> adsorption/desorption isotherms displayed as type II with a H1 hysteresis loop (Fig. S1A), which indicated the mesoporous characteristics of these materials [30]. As shown in Fig. S1B, all samples exhibited the most abundant pore structures around 3.8 nm, although the detailed pore size distributions showed slight difference. As shown in Table 1, the BET surface area for pristine Al<sub>2</sub>O<sub>3</sub> was calculated as 273 m<sup>2</sup>/g, and the loading of Pt decreased the surface area to 238 m<sup>2</sup>/g probably due to the blocking of partial small pores. This can be confirmed by the slightly increased average pore size from 3.2 nm for Al<sub>2</sub>O<sub>3</sub> to 3.6 nm for Pt/Al<sub>2</sub>O<sub>3</sub>. Upon the

post-impregnation of WO<sub>3</sub>, the BET surface area (240 m<sup>2</sup>/g) and average pore size (3.5 nm) barely changed, while the post-impregnation of MgO further decreased the surface area to 202 m<sup>2</sup>/g and increased the average pore size to 3.8 nm. The pore volumes also followed the same trend as BET surface areas, with Al<sub>2</sub>O<sub>3</sub> showing the highest pore volume as 0.33 cm<sup>3</sup>/g, Pt/Al<sub>2</sub>O<sub>3</sub> and WO<sub>3</sub>/Pt/Al<sub>2</sub>O<sub>3</sub> showing the medium pore volume as 0.29 cm<sup>3</sup>/g, and MgO/Pt/Al<sub>2</sub>O<sub>3</sub> showing the lowest pore volume as 0.26 cm<sup>3</sup>/g. It was hypothesized that the impregnated MgO might not only block more small pores from Al<sub>2</sub>O<sub>3</sub> but also cover portion of Pt species. This can be further confirmed by the Pt dispersion measurement using CO pulse titration, which indeed showed that MgO/Pt/Al<sub>2</sub>O<sub>3</sub> possessed lower Pt dispersion (30.1%) than Pt/Al<sub>2</sub>O<sub>3</sub> (54.0%) and WO<sub>3</sub>/Pt/Al<sub>2</sub>O<sub>3</sub> (52.5%). To confirm the Pt dispersion state and the possible Pt tracking with post-impregnated W and Mg species, the HAADF-STEM images and EDS mapping results are shown in Fig. 2. As can be clearly seen from the HAADF-STEM images (Figs. 2-3), no apparent Pt particles could be observed on Pt/Al<sub>2</sub>O<sub>3</sub>, WO<sub>3</sub>/Pt/Al<sub>2</sub>O<sub>3</sub> and MgO/Pt/Al<sub>2</sub>O<sub>3</sub> catalysts, and meanwhile the Pt, W and Mg species were tracking well with Al and O, suggesting a high dispersion of Pt, W and Mg within all catalysts. To further confirm the Pt dispersion state, aberration-corrected HAADF-STEM images for Pt/Al<sub>2</sub>O<sub>3</sub> catalyst have been collected. As shown in Fig. 3e-3h, the Pt atoms were singly dispersed on Al<sub>2</sub>O<sub>3</sub> support within Pt/Al<sub>2</sub>O<sub>3</sub>. In situ DRIFTS of CO adsorption at 25 °C on Pt/Al<sub>2</sub>O<sub>3</sub>, WO<sub>3</sub>/Pt/Al<sub>2</sub>O<sub>3</sub> and MgO/Pt/Al<sub>2</sub>O<sub>3</sub> catalysts was performed, and the results are shown in Fig. 3i. It can be clearly seen that, on all catalysts, only one dominant IR peak ascribed to CO linear vibrational mode at 2098 cm<sup>-1</sup> could be observed [31-33], suggesting that the Pt species within these catalysts were highly dispersed as single atoms. Even after WO<sub>3</sub> and MgO post-impregnation and calcination again, the Pt single atoms were still stably present, although the CO adsorption peak intensity showed some decrease especially for MgO/Pt/Al<sub>2</sub>O<sub>3</sub> due to the covering of Pt species by MgO. Fig. 3j shows the pictures of all samples, in which the

235

236

237

238

239

240

241

242

243

244

245

246

247

248

249

250

251

252

253

254

255

256

257

258

pristine Al<sub>2</sub>O<sub>3</sub> support displayed pure white color as usual, while Pt/Al<sub>2</sub>O<sub>3</sub>, WO<sub>3</sub>/Pt/Al<sub>2</sub>O<sub>3</sub> and MgO/Pt/Al<sub>2</sub>O<sub>3</sub> catalysts all showed light yellowish color, similar to that was observed by Zhang *et al.* for the 0.2 wt.% Pt single atoms loaded on mesoporous Al<sub>2</sub>O<sub>3</sub> [21]. Usually, for Pt/Al<sub>2</sub>O<sub>3</sub> catalysts containing Pt nanoparticles, the sample color would be much darker such as dark gray or even black, which was not the case at all for the studied catalysts in this work. Above-mentioned results suggest that the Pt species within all catalysts was indeed highly dispersed on  $\eta$ -Al<sub>2</sub>O<sub>3</sub> support as single atoms, which can be further verified by the following XAS results for Pt L<sub>III</sub>-edge.

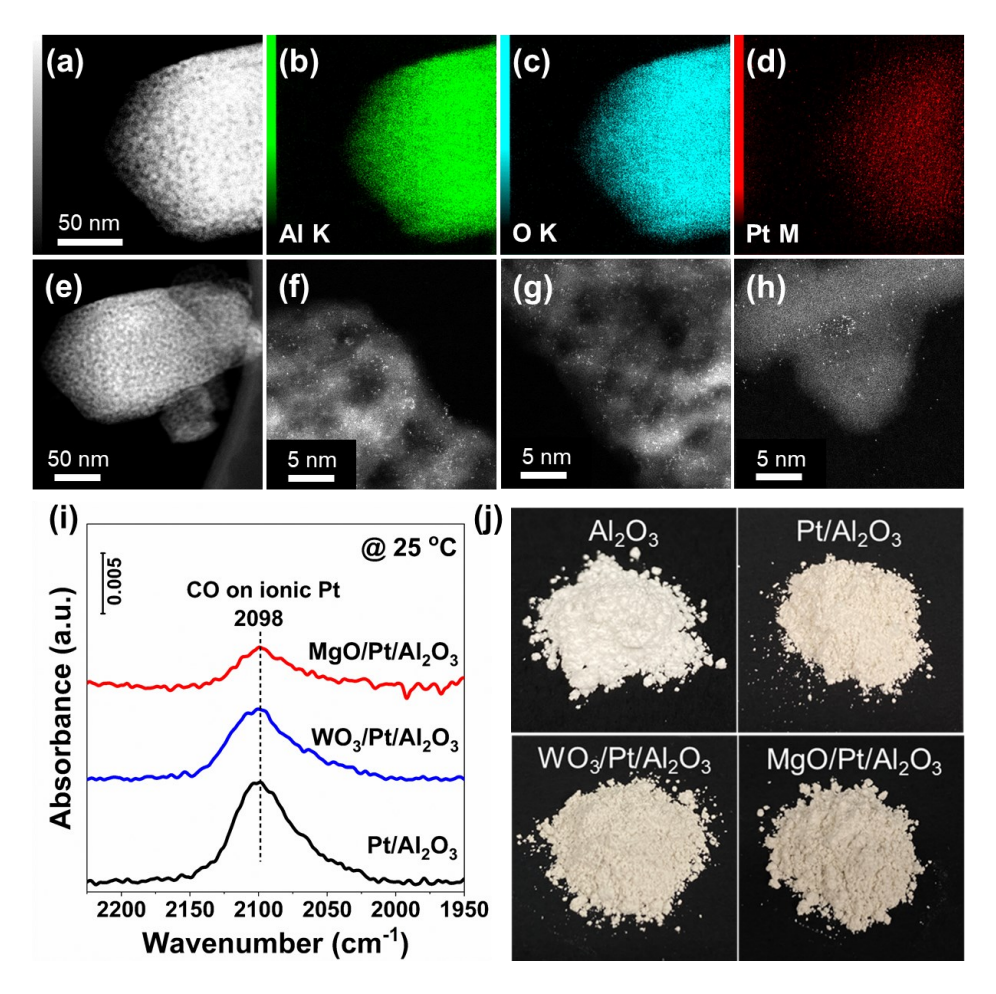


**Fig. 3.** (a-h) HAADF AC-STEM and EDS mapping results for Pt/Al<sub>2</sub>O<sub>3</sub>; (i) *In situ* DRIFTS of CO adsorption at 25 °C on Pt/Al<sub>2</sub>O<sub>3</sub>, WO<sub>3</sub>/Pt/Al<sub>2</sub>O<sub>3</sub> and MgO/Pt/Al<sub>2</sub>O<sub>3</sub>; and (j) Pictures of pristine Al<sub>2</sub>O<sub>3</sub> support, as well as Pt/Al<sub>2</sub>O<sub>3</sub>, WO<sub>3</sub>/Pt/Al<sub>2</sub>O<sub>3</sub> and MgO/Pt/Al<sub>2</sub>O<sub>3</sub> catalysts.

Fig. 4A shows the normalized XANES for Pt L<sub>III</sub>-edge in Pt foil, Pt/Al<sub>2</sub>O<sub>3</sub>, MgO/Pt/Al<sub>2</sub>O<sub>3</sub>,

and PtO<sub>2</sub> samples. It has to be noted that the XAS for Pt L<sub>III</sub>-edge in WO<sub>3</sub>/Pt/Al<sub>2</sub>O<sub>3</sub> catalyst could not be measured due to the overlap of adsorption edge energy for W L<sub>II</sub>-edge and Pt L<sub>III</sub>edge. From the white line intensity of normalized XANES for Pt L<sub>III</sub>-edge, it can be concluded that the Pt species in Pt/Al<sub>2</sub>O<sub>3</sub> and MgO/Pt/Al<sub>2</sub>O<sub>3</sub> catalysts was in the highest oxidation state of Pt<sup>4+</sup>, which can also be confirmed by the first-order derivatives of XANES in Fig. 4B where the maximum value of first-order derivatives of Pt L<sub>III</sub>-edge XANES for Pt/Al<sub>2</sub>O<sub>3</sub> and MgO/Pt/Al<sub>2</sub>O<sub>3</sub> catalysts were almost the same as that for PtO<sub>2</sub> reference. For easy comparison, Fig. 4C shows the Fourier transformed  $k^2$ -weighted EXAFS oscillations in R space without vertical shift for Pt L<sub>III</sub>-edge in Pt foil, Pt/Al<sub>2</sub>O<sub>3</sub>, MgO/Pt/Al<sub>2</sub>O<sub>3</sub> and PtO<sub>2</sub> samples, and the corresponding EXAFS curve fitting results are presented in Fig. S2 and Table 2. For Pt/Al<sub>2</sub>O<sub>3</sub> and MgO/Pt/Al<sub>2</sub>O<sub>3</sub> catalysts, it was first confirmed that no metallic Pt-Pt was present. The first coordination shell can be ascribed to Pt-O with the bond length at 1.99 Å, slightly shorter than that in PtO<sub>2</sub> reference (2.02 Å). The second coordination shell can be ascribed to Pt-O-Al in Pt/Al<sub>2</sub>O<sub>3</sub> at 3.20 Å and Pt-O-Al/Mg at 3.21 Å, both being longer than that of Pt-O-Pt in PtO<sub>2</sub> reference (3.07 Å). Since Mg and Al are elements close to each other, it is very difficult to discern the two during the EXAFS curve fitting. However, the possible strong interaction between Pt and MgO can be verified by the coordination number of Pt-O-Al/Mg (6.0) in MgO/Pt/Al<sub>2</sub>O<sub>3</sub>, which was higher than that of Pt-O-Al (5.0) in Pt/Al<sub>2</sub>O<sub>3</sub>.

273

274

275

276

277

278

279

280

281

282

283

284

285

286

287

288

289

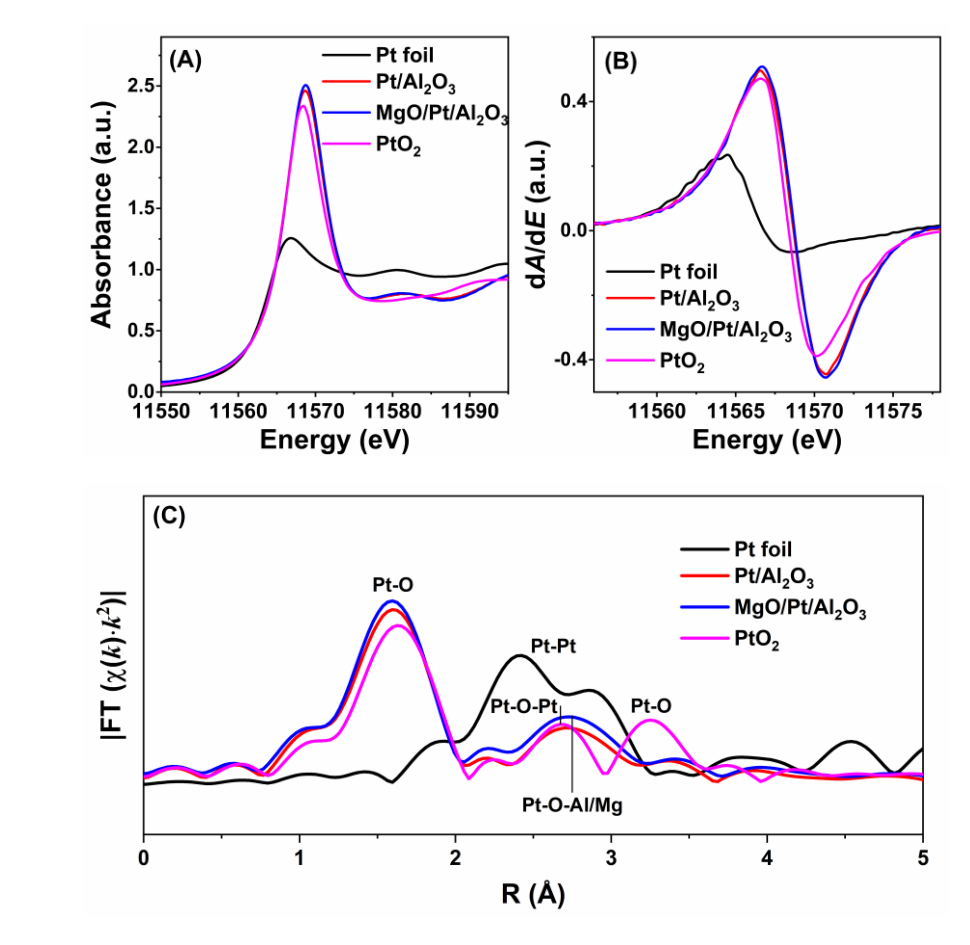


Fig. 4. (A) Normalized XANES, (B) first-order derivatives of XANES and (C) Fourier transformed  $k^2$ -weighted EXAFS oscillations in R space for Pt L<sub>III</sub>-edge in Pt foil, Pt/Al<sub>2</sub>O<sub>3</sub>, MgO/Pt/Al<sub>2</sub>O<sub>3</sub> and PtO<sub>2</sub> samples.

**Table 2.** Pt L<sub>III</sub>-edge EXAFS fitting parameters for Pt-based catalysts and Pt foil, PtO<sub>2</sub> references (k range = 3.0-11.0 Å<sup>-1</sup> for Fourier transform)

Sample	Shell	CN	R (Å)	ΔE <sub>0</sub> (eV)	$\sigma^2 (10^{-3} \text{ Å}^2)$	R factor
Pt foil	Pt-Pt	$12.0 \pm 0.9$	$2.76 \pm 0.01$	$7.3 \pm 0.6$	$4.12 \pm 0.54$	0.006
PtO <sub>2</sub>	Pt-O	$6.0 \pm 0.8$	$2.02 \pm 0.01$	$10.7 \pm 1.3$	$1.12 \pm 1.54$	
	Pt-O-Pt	$6.0 \pm 0.8$	$3.07 \pm 0.04$	$6.2 \pm 5.5$	$5.18 \pm 2.17$	0.012
	Pt-O	$12.0\pm1.5$	$3.71\pm0.05$	$13.6 \pm 2.5$	$6.33 \pm 4.48$	
Pt/Al <sub>2</sub> O <sub>3</sub>	Pt-O	$6.3 \pm 1.1$	$1.99 \pm 0.01$	$10.7 \pm 1.3$	$0.47 \pm 1.81$	0.021
	Pt-O-Al	$5.0\pm2.4$	$3.20\pm0.05$	$14.9 \pm 5.5$	$0.94 \pm 3.62$	
MgO/Pt/Al <sub>2</sub> O <sub>3</sub>	Pt-O	$6.6 \pm 0.9$	$1.99 \pm 0.01$	$10.7 \pm 1.3$	$0.65 \pm 1.53$	0.019
	Pt-O-Al/Mg	$6.0 \pm 1.4$	$3.21 \pm 0.02$	$14.9 \pm 5.5$	$0.94 \pm 3.62$	

Although the valence state and local coordination structure of Pt species in WO<sub>3</sub>/Pt/Al<sub>2</sub>O<sub>3</sub> could not be determined by Pt L<sub>III</sub>-edge XAS, the information of W species in this catalyst could actually be obtained using W L<sub>III</sub>-edge XAS. Fig. 5A shows the normalized XANES for W L<sub>III</sub>-edge in W foil, WO<sub>3</sub>/Pt/Al<sub>2</sub>O<sub>3</sub> and WO<sub>3</sub>, which suggested that the W species in WO<sub>3</sub>/Pt/Al<sub>2</sub>O<sub>3</sub> catalyst possessed the oxidation state very close to that in WO<sub>3</sub>. From the firstorder derivatives of W L<sub>III</sub>-edge XANES in Fig. 5B, the W species in WO<sub>3</sub>/Pt/Al<sub>2</sub>O<sub>3</sub> catalyst (with absorption edge energy at 10208.9 eV) showed slightly lower oxidation state than that in pure WO<sub>3</sub> (with absorption edge energy at 10209.2 eV). Furthermore, Fig. 5C shows the second-order derivatives of W L<sub>III</sub>-edge XANES to better discern the two split peak positions in the white line. Accordingly, the gap energy between the two subpeaks at higher and lower energy positions could be determined, which was measured as 4.0 eV for WO<sub>3</sub> reference and 3.4 eV for WO<sub>3</sub>/Pt/Al<sub>2</sub>O<sub>3</sub> catalyst. It was reported that such gap energy between the two subpeaks for W L<sub>III</sub>-edge XANES would decrease if the local coordination structure of W species changing from octahedron -WO<sub>6</sub> to tetrahedron -WO<sub>4</sub> [34]. Therefore, it can be concluded that, due to the high dispersion of W species within WO<sub>3</sub>/Pt/Al<sub>2</sub>O<sub>3</sub> catalyst (judged from XRD results), a portion of W species was present as tetrahedron -WO<sub>4</sub> besides of octahedron -WO<sub>6</sub> thus leading to rich defective  $W^{(6-\delta)+}O_x$  sites with the average valence state lower than W<sup>6+</sup>O<sub>x</sub> in pure WO<sub>3</sub>. This can be verified by the W L<sub>III</sub>-edge EXAFS results in R space (Fig. 5D) and the corresponding curve fitting results (Fig. S3 and Table S1). For WO<sub>3</sub> reference, the first W-O shell possessed the coordination number as 6.0, with the W-O multiple scattering peak and the W-O-W coordination shell clearly showing up. However, for WO<sub>3</sub>/Pt/Al<sub>2</sub>O<sub>3</sub> catalyst, the W-O shell possessed the coordination number as 5.1, and no clear W-O multiple scattering peak and W-O-W coordination shell could be observed. This further confirmed that the WO<sub>x</sub> species within WO<sub>3</sub>/Pt/Al<sub>2</sub>O<sub>3</sub> catalyst was indeed highly dispersed with rich defects, which was probably beneficial for reactant adsorption and activation during

298

299

300

301

302

303

304

305

306

307

308

309

310

311

312

313

314

315

316

317

318

319

320

321

### 323 certain catalysis reactions.

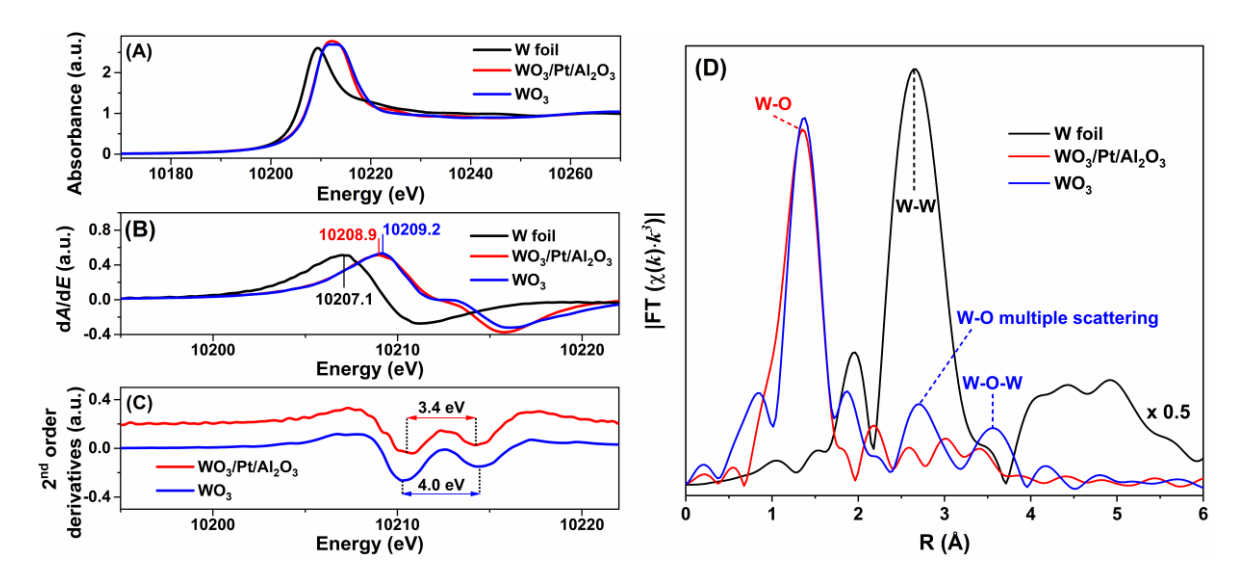


**Fig. 5.** (A) Normalized XANES, (B) first-order derivatives of XANES, (C) second-order derivatives of XANES, and (D) Fourier transformed  $k^3$ -weighted EXAFS oscillations in R space for W L<sub>III</sub>-edge in W foil, WO<sub>3</sub>/Pt/Al<sub>2</sub>O<sub>3</sub> and WO<sub>3</sub> samples.

# 3.2. Surface acidity characterization

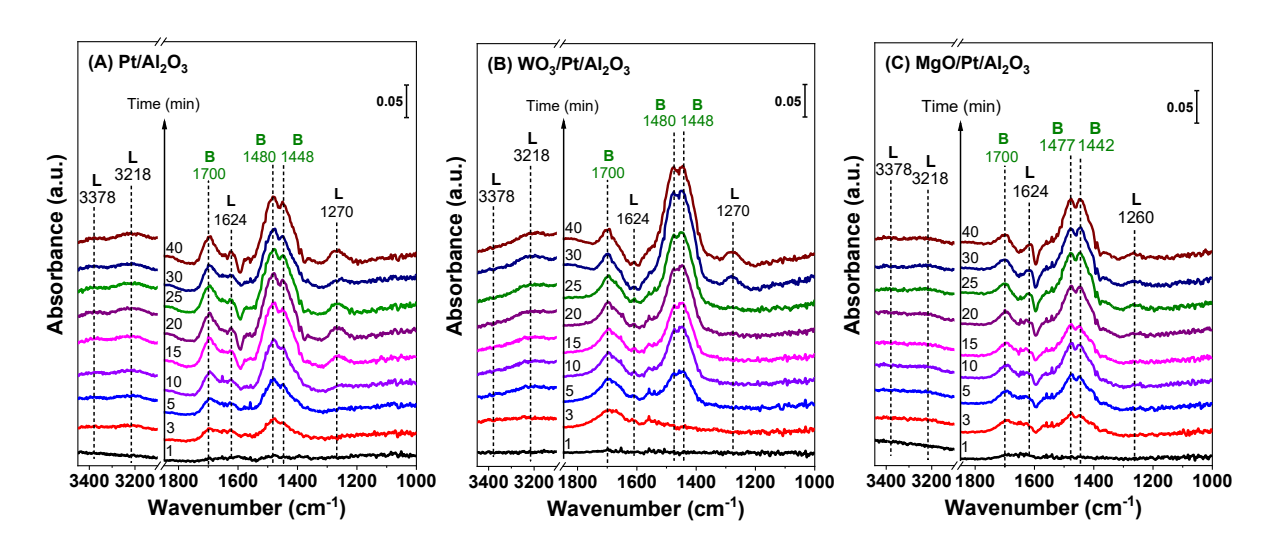


**Fig. 6.** In situ DRIFTS of NH<sub>3</sub> adsorption at 50 °C on Pt/Al<sub>2</sub>O<sub>3</sub>, WO<sub>3</sub>/Pt/Al<sub>2</sub>O<sub>3</sub> and MgO/Pt/Al<sub>2</sub>O<sub>3</sub> catalysts.

In order to characterize the surface acidity of different catalysts, *in situ* DRIFTS of NH<sub>3</sub> adsorption at 50 °C on Pt/Al<sub>2</sub>O<sub>3</sub>, WO<sub>3</sub>/Pt/Al<sub>2</sub>O<sub>3</sub> and MgO/Pt/Al<sub>2</sub>O<sub>3</sub> were performed, followed

by NH<sub>3</sub> desorption at elevated temperatures. As shown in **Fig. 6**, upon the introduction of NH<sub>3</sub> at 50 °C, the NH<sub>3</sub> adsorbed species bound to Lewis acid sites (1270/1260, 1624, 3218, and 3378 cm<sup>-1</sup>) and NH<sub>4</sub><sup>+</sup> adsorbed species bound to Brønsted acid sites (1442/1448, 1477/1480, and 1700 cm<sup>-1</sup>) both showed monotonic increase as a function of time and reached steady state after 30 min [35-37]. It is obvious that the intensity of the peaks at 1448 and 1480 cm<sup>-1</sup> on WO<sub>3</sub>/Pt/Al<sub>2</sub>O<sub>3</sub> ascribed to NH<sub>4</sub><sup>+</sup> on Brønsted acid sites were much higher than those on Pt/Al<sub>2</sub>O<sub>3</sub>, indicating the improved surface acidity of catalyst by WO<sub>3</sub> addition. In contrast, both the NH<sub>3</sub> species bound to Lewis acid sites and NH<sub>4</sub><sup>+</sup> species bound to Brønsted acid sites on MgO/Pt/Al<sub>2</sub>O<sub>3</sub> showed some peak intensity decrease comparing to those on Pt/Al<sub>2</sub>O<sub>3</sub>, indicating that the basic MgO addition indeed decreased the surface acidity of catalyst to a certain extent. The *in situ* DRIFTS of NH<sub>3</sub> desorption at different temperatures (**Fig. S4**) also confirmed that the surface acid strength of the studied catalysts followed such sequence: WO<sub>3</sub>/Pt/Al<sub>2</sub>O<sub>3</sub> > Pt/Al<sub>2</sub>O<sub>3</sub> > MgO/Pt/Al<sub>2</sub>O<sub>3</sub>.

### 3.3. Catalyst reducibility characterization

To study the reducibility of Pt species, H<sub>2</sub>-TPR profiles were measured for Al<sub>2</sub>O<sub>3</sub> support, Pt/Al<sub>2</sub>O<sub>3</sub>, WO<sub>3</sub>/Pt/Al<sub>2</sub>O<sub>3</sub> and MgO/Pt/Al<sub>2</sub>O<sub>3</sub> catalysts. As shown in **Fig. 7**, the pure Al<sub>2</sub>O<sub>3</sub> support did not have obvious H<sub>2</sub> consumption up to 500 °C. For all Pt containing catalysts, three H<sub>2</sub> consumption bands showed up, at *ca.* 94-110, 214-223, and 390-460 °C. According to literature [38, 39], the first peak was attributed to the reduction of adsorbed surface oxygen species, and the second one and third one were assigned to the reduction of PtO<sub>x</sub> species weakly and strongly interacting with Al<sub>2</sub>O<sub>3</sub> support. As verified above, Pt was present as single atoms within the Pt/Al<sub>2</sub>O<sub>3</sub> catalyst, therefore the reduction peaks for PtO<sub>x</sub> species in this work can be actually assigned to the reduction of Pt-O-Al species specifically. Different from the intense reduction of weakly interacted PtO<sub>x</sub> species from Pt particles loaded on Al<sub>2</sub>O<sub>3</sub> as reported elsewhere [38, 39], much more intense reduction peak for PtO<sub>x</sub> species strongly interacting

with Al<sub>2</sub>O<sub>3</sub> support was observed on the Pt/Al<sub>2</sub>O<sub>3</sub> catalyst in this work, which was mainly due to the atomic dispersion of Pt species on η-Al<sub>2</sub>O<sub>3</sub> to form Pt-O-Al bonds. After modification by WO<sub>3</sub> and MgO, the first and second reduction peaks for Pt/Al<sub>2</sub>O<sub>3</sub> slightly shifted to higher temperatures, possibly indicating some enhanced interaction between Pt and Al<sub>2</sub>O<sub>3</sub> upon the WO<sub>3</sub> or MgO addition. In addition, with the continuous reduction of Pt-O in Pt-O-Al/Mg/W bonds, broad reduction peaks showed up for all catalysts. By quantitatively analyzing the reduction peaks in H<sub>2</sub>-TPR profiles, the H<sub>2</sub> consumption for different species was calculated and the results are shown in **Table S2**. The H<sub>2</sub> consumption on Pt/Al<sub>2</sub>O<sub>3</sub> (122.3 μmol/g) was greatly increased after WO<sub>3</sub> addition (167.3 μmol/g), while it was decreased after MgO modification (70.1 μmol/g). Different interactions between Pt and WO<sub>3</sub> or MgO should be present, resulting in the different reducibility of Pt species.

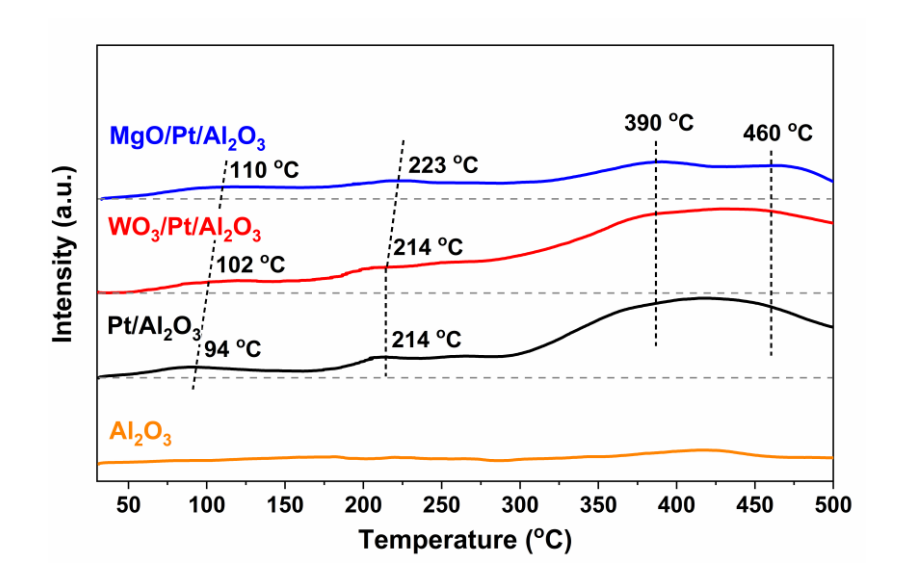


**Fig. 7.** H<sub>2</sub>-TPR profiles of Al<sub>2</sub>O<sub>3</sub> support, Pt/Al<sub>2</sub>O<sub>3</sub>, WO<sub>3</sub>/Pt/Al<sub>2</sub>O<sub>3</sub> and MgO/Pt/Al<sub>2</sub>O<sub>3</sub> catalysts.

### 3.4. Surface property characterization

Surface species and surface element compositions on different catalysts were determined by XPS technique. **Fig. 8** illustrates the Pt 4d and O 1s XPS spectra, and the surface element compositions and O<sub>ads</sub>/O<sub>latt</sub> ratio are summarized in **Table S3**. As expected, with the loading of

WO<sub>3</sub> and MgO onto Pt/Al<sub>2</sub>O<sub>3</sub>, both surface Al and Pt concentrations decreased to a certain extent due to the covering of Pt/Al<sub>2</sub>O<sub>3</sub> surface, particularly after MgO loading. The trend of surface Pt concentration was in consistence with Pt dispersion on all catalysts measured by CO pulse titration. It can be clearly seen from Fig. 8A that only Pt4+ species were present in Pt/Al<sub>2</sub>O<sub>3</sub> and WO<sub>3</sub>/Pt/Al<sub>2</sub>O<sub>3</sub> catalysts [40]. It should be noted that it was not possible to discern the Pt species in MgO/Pt/Al<sub>2</sub>O<sub>3</sub> catalyst due to the overlap of Pt 4f/4d with Mg<sub>Auger</sub> and Al 2p signals. As for the O 1s XPS (Fig. 8B), the asymmetrical O 1s spectrum for each catalyst could be deconvoluted into two components, with the surface lattice oxygen (O<sub>latt</sub>) species at BE = 530.9 eV and the surface adsorbed oxygen ( $O_{ads}$ ) species at BE = 532.5 eV [41, 42]. As shown in **Table S3**, the surface O<sub>ads</sub>/O<sub>latt</sub> molar ratio decreased in the order of WO<sub>3</sub>/Pt/Al<sub>2</sub>O<sub>3</sub> (0.77) > MgO/Pt/Al<sub>2</sub>O<sub>3</sub> (0.32) > Pt/Al<sub>2</sub>O<sub>3</sub> (0.17). A higher concentration of O<sub>ads</sub> species could be related to a higher density of surface oxygen vacancy (Ovac) on a particular catalyst. Since WO3 and MgO were highly dispersed once loaded onto Pt/Al<sub>2</sub>O<sub>3</sub>, it was reasonable that higher concentration of Ovac could be formed on WO3 and MgO modified catalysts thus possibly leading to the formation of more O<sub>ads</sub> species especially the acidic hydroxyls on WO<sub>3</sub>/Pt/Al<sub>2</sub>O<sub>3</sub> and basic hydroxyls on MgO/Pt/Al<sub>2</sub>O<sub>3</sub>.

377

378

379

380

381

382

383

384

385

386

387

388

389

390

391

392

393

394

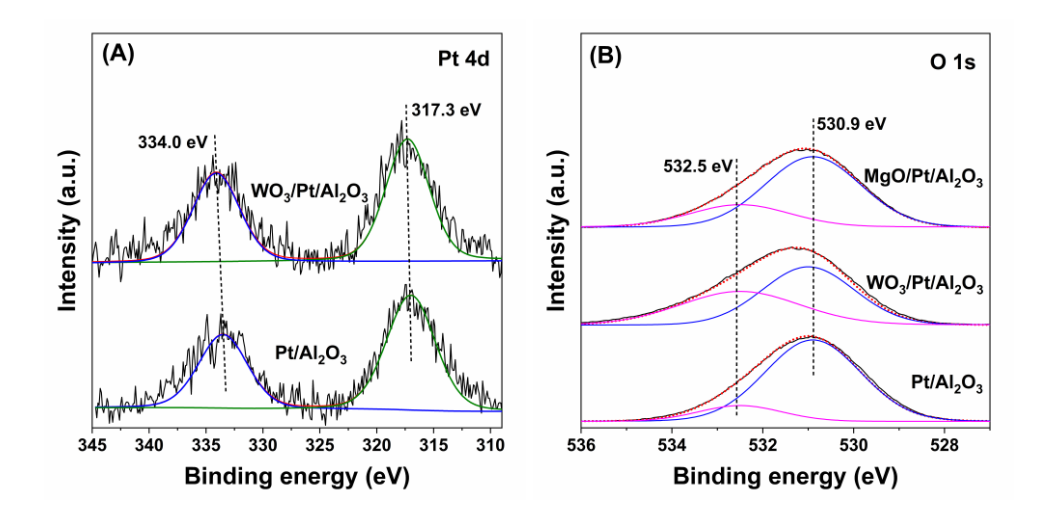


**Fig. 8.** (A) Pt 4d XPS and (B) O 1s XPS for Pt/Al<sub>2</sub>O<sub>3</sub>, WO<sub>3</sub>/Pt/Al<sub>2</sub>O<sub>2</sub> and MgO/Pt/Al<sub>2</sub>O<sub>3</sub> catalysts.

# 3.5. Catalytic performance for CO oxidation

396

397

398

399

400

401

402

403

404

405

406

407

408

409

410

411

412

413

414

415

416

417

418

To evaluate the catalytic performance of different catalysts, the supports including Al<sub>2</sub>O<sub>3</sub>, and WO<sub>3</sub>, MgO modified Al<sub>2</sub>O<sub>3</sub> were first tested for CO oxidation (Fig. S5). For the supports without Pt, their catalytic CO oxidation performance was very poor as expected, following such sequence: WO<sub>3</sub>/Al<sub>2</sub>O<sub>3</sub> > MgO/Al<sub>2</sub>O<sub>3</sub> > Al<sub>2</sub>O<sub>3</sub>. Upon 1% Pt loading, the CO oxidation performance showed significant enhancement, with the T<sub>50</sub> (the temperature at which the CO conversion reaching 50%) decreased by ca. 150 °C. However, as shown in Fig. 9, for the CO oxidation in dry condition, the WO<sub>3</sub> and MgO modification for Pt/Al<sub>2</sub>O<sub>3</sub> catalyst showed some negative effect on CO oxidation performance, possibly due to the covering of partial Pt sites during the post-impregnation procedure. Yet, it is interesting to see that the introduction of 5% H<sub>2</sub>O into the CO oxidation reaction stream showed positive effect on improving the catalytic performance, and the H<sub>2</sub>O promotion effect was much more significant on MgO/Pt/Al<sub>2</sub>O<sub>3</sub> catalyst than that on Pt/Al<sub>2</sub>O<sub>3</sub> and WO<sub>3</sub>/Pt/Al<sub>2</sub>O<sub>3</sub> catalysts. In most practical applications involving CO oxidation such as the diesel oxidation catalysts and three-way catalysts for vehicle emission control, the reaction conditions always contain H<sub>2</sub>O, and using basic metal oxides such as MgO to modify the Pt based catalysts should be an effective way to enhance the CO oxidation performance. The promotion effect of MgO addition on Pt/Al<sub>2</sub>O<sub>3</sub> catalyst for CO oxidation can be well explained using the *in situ* DRIFTS results as descried below. To check the stability of Pt single atoms after CO oxidation at 300 °C, in situ DRIFTS of CO adsorption on the spent Pt/Al<sub>2</sub>O<sub>3</sub> catalyst was collected at 25 °C and shown in Fig. S6A. Other than a dominant peak at 2098 cm<sup>-1</sup> for CO adsorption on Pt single atoms, a shoulder peak at 2050 cm<sup>-1</sup> <sup>1</sup> due to the CO adsorption on Pt clusters also showed up on the spent catalyst, suggesting that a portion of Pt single atoms had transformed into Pt clusters during the CO oxidation reaction.

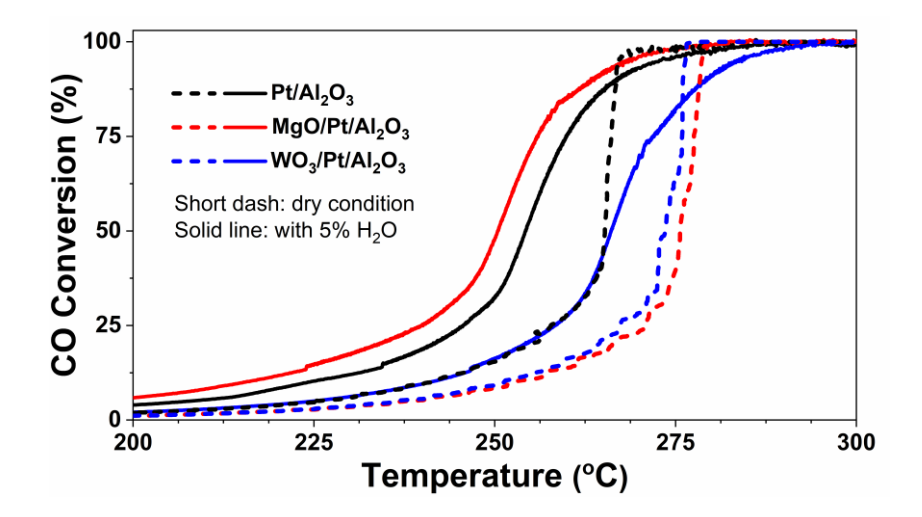


Fig. 9. CO oxidation activity on Pt/Al<sub>2</sub>O<sub>3</sub>, WO<sub>3</sub>/Pt/Al<sub>2</sub>O<sub>3</sub>, MgO/Pt/Al<sub>2</sub>O<sub>3</sub> catalysts without and with the presence of H<sub>2</sub>O in the reaction stream. Conditions: [CO] = [O<sub>2</sub>] = 1%, 5% H<sub>2</sub>O if used, balanced with Ar, WHSV of 200,000 mL· $g_{cat}^{-1}$ ·h<sup>-1</sup>, temperature ramp of 2 °C/min from 200 to 300 °C.

### 3.6. In situ DRIFTS study for CO oxidation

In situ DRIFTS experiments of CO oxidation under conditions without and with H<sub>2</sub>O were performed at 200 °C on all catalysts. It can be observed from Figs. S7 and 10 that adsorbates appeared on all the catalysts after the exposure to reaction flow. For CO oxidation on Pt/Al<sub>2</sub>O<sub>3</sub> under dry condition (Fig. S7A), the appearance of bands at 2172 and 2067 cm<sup>-1</sup> was due to the gas phase CO and CO adsorbed on Pt sites [13, 14], and bands at 1655 and 1440 cm<sup>-1</sup> were attributed to the surface bicarbonate species on Al<sub>2</sub>O<sub>3</sub> support [43], where the bicarbonate came from the CO<sub>2</sub> produced in CO oxidation. Comparing to Pt/Al<sub>2</sub>O<sub>3</sub>, less adsorbed CO and bicarbonate species were observed on WO<sub>3</sub>/Pt/Al<sub>2</sub>O<sub>3</sub> under dry CO oxidation condition (Fig. S7B) due to a less exposure of Pt and Al<sub>2</sub>O<sub>3</sub> and the enhanced surface acidity as well. As depicted in Fig. S7C, on MgO/Pt/Al<sub>2</sub>O<sub>3</sub>, less CO species adsorbed on Pt sites was also observed comparing to that on Pt/Al<sub>2</sub>O<sub>3</sub>. However, more bicarbonate species was present on MgO/Pt/Al<sub>2</sub>O<sub>3</sub> probably due to the enhanced surface basicity, also with a new band at 1590 cm<sup>-1</sup> corresponding to formate species showing up [44]. As shown in Fig. S8, after cutting off

CO (in dry condition), the CO adsorbed species on Pt sites disappeared rapidly, and the adsorbed carbonates could partially desorb from the catalysts. It should be noted that there was still a large amount of residual carbonates on the catalysts even after flowing O<sub>2</sub> for 40 min especially on MgO/Pt/Al<sub>2</sub>O<sub>3</sub>, which might block the Pt active sites from efficient catalytic cycling. Comparing to CO oxidation under dry condition, as shown in Fig. 10, clear bands at 2352 cm<sup>-1</sup> due to adsorbed CO<sub>2</sub> appeared on all the catalysts with the presence of H<sub>2</sub>O in reaction stream at the same temperature (200 °C), indicating an improved catalytic activity for CO oxidation to CO<sub>2</sub> by H<sub>2</sub>O. This agreed well with the CO oxidation results in Fig. 9. Interestingly, instead of abundant surface bicarbonate species, very little formate species (1592) and 1377 cm<sup>-1</sup>) on Pt/Al<sub>2</sub>O<sub>3</sub> (Fig. 10A) and almost no species on WO<sub>3</sub>/Pt/Al<sub>2</sub>O<sub>3</sub> (Fig. 10B) were observed under the testing condition with H<sub>2</sub>O. In other words, the addition of H<sub>2</sub>O inhibited the formation of bicarbonates on these two catalysts, which could help the cycling of Pt sites during CO oxidation. Different from Pt/Al<sub>2</sub>O<sub>3</sub> and WO<sub>3</sub>/Pt/Al<sub>2</sub>O<sub>3</sub>, both bicarbonates and formate species were largely present on MgO/Pt/Al<sub>2</sub>O<sub>3</sub> due to its basic nature (**Fig. 10C**). However, the carbonate species desorbed quickly on MgO/Pt/Al<sub>2</sub>O<sub>3</sub> once the CO was cut off (Fig. S9). This result suggests that the introduced H<sub>2</sub>O promoted the desorption of formed carbonate species and possibly formed reactive hydroxyls as well, thus facilitating the CO oxidation cycle significantly on the MgO/Pt/Al<sub>2</sub>O<sub>3</sub> catalyst. It has been reported that OH species not only can participate as a reactant for CO oxidation but also can act as a promoter when they are located at/or nearby Pt sites,[32] with which the CO oxidation can follow H<sub>2</sub>Omediated Langmuir-Hinshelwood mechanism. [45] Due to the basic nature of MgO, abundant reactive hydroxyls could be formed on MgO/Pt/Al<sub>2</sub>O<sub>3</sub> surface with which the CO oxidation activity could be largely enhanced due to the improved O<sub>2</sub> activation in the presence of H<sub>2</sub>O, even though the in situ formed bicarbonates and formate species might block some Pt sites.

438

439

440

441

442

443

444

445

446

447

448

449

450

451

452

453

454

455

456

457

458

459

460

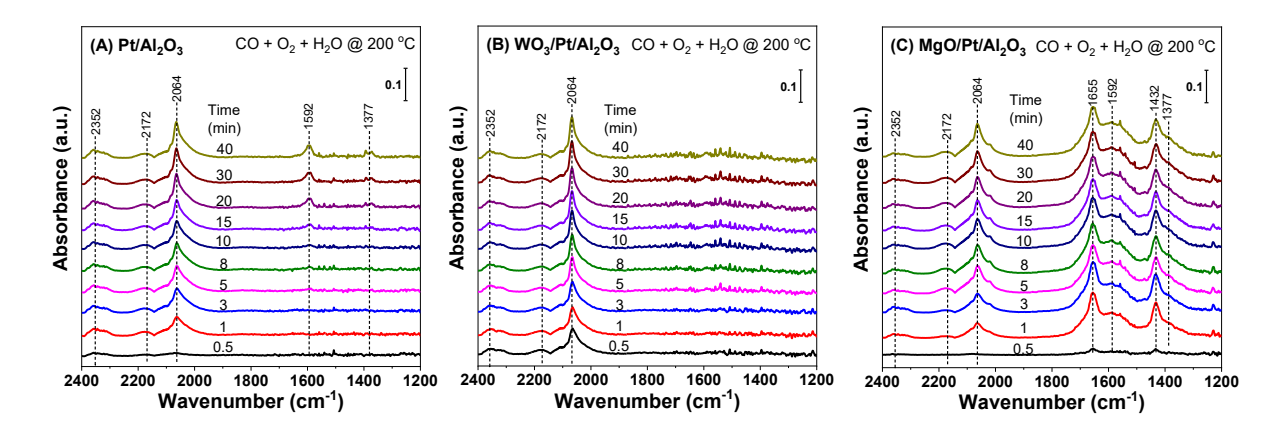


**Figure 10.** In situ DRIFTS of CO oxidation as a function of exposure time to  $CO + O_2 + H_2O$  flow at 200 °C on the samples.

# 3.7. Catalytic performance for methanol decomposition

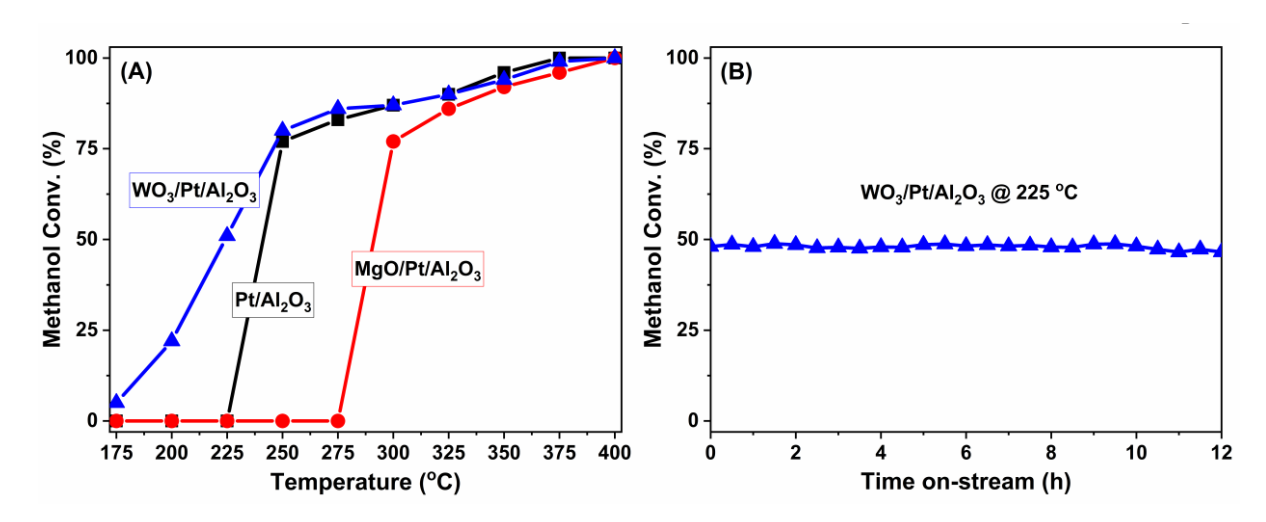
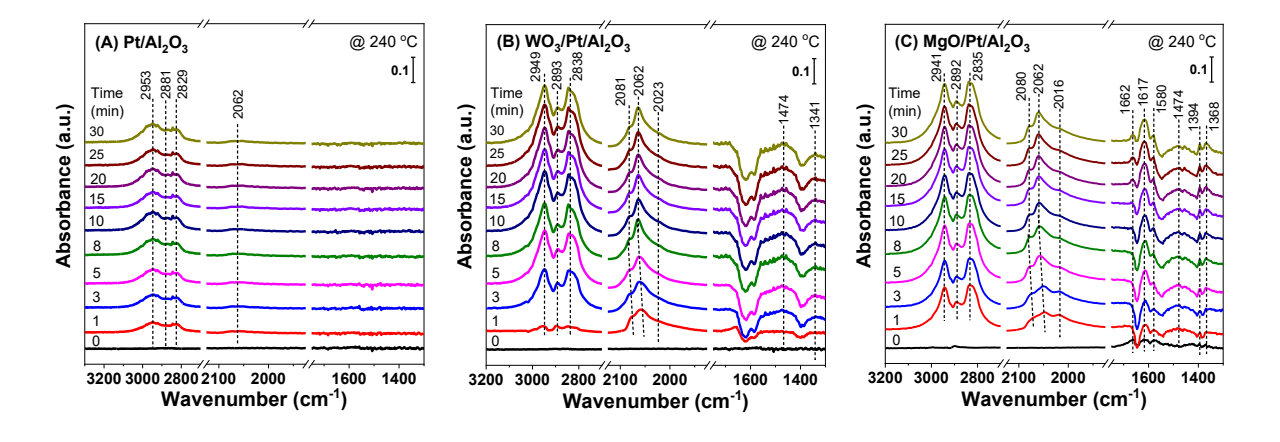


**Fig. 11.** (A) Methanol decomposition activity on Pt/Al<sub>2</sub>O<sub>3</sub>, WO<sub>3</sub>/Pt/Al<sub>2</sub>O<sub>3</sub>, and MgO/Pt/Al<sub>2</sub>O<sub>3</sub>; (B) Catalytic stability of WO<sub>3</sub>/Pt/Al<sub>2</sub>O<sub>3</sub> catalyst for methanol decomposition at 225 °C. Conditions: 10% CH<sub>3</sub>OH, balanced with Ar, WHSV = 50,000 mL·g<sub>cat</sub>-1·h<sup>-1</sup>.

As an efficient hydrogen carrier, methanol is relatively inexpensive and can be manufactured from a variety of sources [10, 46]. Looking for highly effective catalysts for methanol decomposition to release H<sub>2</sub> quickly is of significant importance. Therefore, the Pt/Al<sub>2</sub>O<sub>3</sub>, WO<sub>3</sub>/Pt/Al<sub>2</sub>O<sub>3</sub> and MgO/Pt/Al<sub>2</sub>O<sub>3</sub> catalysts were also tested for methanol direct decomposition reaction. As shown in **Fig. 11A**, WO<sub>3</sub>/Pt/Al<sub>2</sub>O<sub>3</sub> catalyst showed much higher methanol

decomposition activity than Pt/Al<sub>2</sub>O<sub>3</sub> catalyst below 250 °C, while the MgO/Pt/Al<sub>2</sub>O<sub>3</sub> catalyst showed much lower methanol decomposition activity than Pt/Al<sub>2</sub>O<sub>3</sub> catalyst (with the T<sub>50</sub> of methanol conversion shifted ca. 50 °C to higher temperature range). It is obvious that the addition of acidic WO<sub>3</sub> significantly improved the catalytic performance of Pt/Al<sub>2</sub>O<sub>3</sub> catalyst for methanol decomposition, and such excellent methanol decomposition activity on WO<sub>3</sub>/Pt/Al<sub>2</sub>O<sub>3</sub> catalyst could be well maintained during the long-term catalytic stability testing at 225 °C (Fig. 11B). To reveal the stability of Pt single atoms during long-term methanol decomposition at 225 °C for 12 h, in situ DRIFTS of CO adsorption on the spent WO<sub>3</sub>/Pt/Al<sub>2</sub>O<sub>3</sub> catalyst was conducted at 25 °C. As shown in Fig. S6B, a shoulder peak for CO adsorption on Pt clusters was observed on the spent catalyst, implying that a portion of Pt single atoms were transformed into Pt clusters probably due to the in situ reduction by the produced H<sub>2</sub> in methanol decomposition. It was reported that Pt single-atoms were more active in methanol decomposition than Pt clusters.[10] Based on the undetectable decline of methanol decomposition activity in the long-term testing, there should be only a very small portion of Pt single-atoms converted into clusters during this process. To understand the intrinsic mechanisms of promotion effect from WO<sub>3</sub> and inhibition effect from MgO on Pt/Al<sub>2</sub>O<sub>3</sub> catalyst for methanol decomposition, systematic in situ DRIFTS of methanol decomposition and desorption was performed as described below in detail.

# 3.8. In situ DRIFTS study for methanol decomposition



475

476

477

478

479

480

481

482

483

484

485

486

487

488

489

490

491

492

**Fig. 12.** *In situ* DRIFTS of methanol decomposition at 240 °C on Pt/Al<sub>2</sub>O<sub>3</sub>, WO<sub>3</sub>/Pt/Al<sub>2</sub>O<sub>3</sub> and MgO/Pt/Al<sub>2</sub>O<sub>3</sub> catalysts.

495

496

497

498

499

500

501

502

503

504

505

506

507

508

509

510

511

512

513

514

515

516

517

518

519

*In situ* DRIFTS of methanol decomposition at 240 °C over the catalysts are shown in Fig. 12. As shown in Fig. 12A, once exposure to methanol, the bands at 2828-2949 cm<sup>-1</sup> attributed to the C-H vibration of methoxy group and the bands at 2062 cm<sup>-1</sup> assigned to CO linearly adsorbed on Pt sites appeared immediately on Pt/Al<sub>2</sub>O<sub>3</sub> [47]. After modification by WO<sub>3</sub> and MgO, the adsorption of methoxy group and CO species showed obvious increase. As indicated by O 1s XPS results, WO<sub>3</sub> and MgO modified Pt/Al<sub>2</sub>O<sub>3</sub> catalysts possessed more O<sub>vac</sub> than Pt/Al<sub>2</sub>O<sub>3</sub>, which could be considered responsible for the higher adsorption of methanol and in situ formed CO species on them. In addition, different from that on Pt/Al<sub>2</sub>O<sub>3</sub>, the bands at 1474 and 1341/1368 cm<sup>-1</sup> ascribed to C-O vibration within methoxy group was observed on both WO<sub>3</sub>/Pt/Al<sub>2</sub>O<sub>3</sub> and MgO/Pt/Al<sub>2</sub>O<sub>3</sub> catalysts probably due to the intense adsorption of methanol (Fig. 12A and 12B). Comparing to Pt/Al<sub>2</sub>O<sub>3</sub> and WO<sub>3</sub>/Pt/Al<sub>2</sub>O<sub>3</sub>, the peaks at 1662, 1617, 1580 and 1394 cm<sup>-1</sup> showed up on MgO/Pt/Al<sub>2</sub>O<sub>3</sub> due to the OCO stretching mode of carbonate species formed during methanol decomposition [47]. Once cutting off the methanol, as depicted in Fig. 13, the adsorbed methoxy group decreased, but the adsorbed CO species remained over all the catalysts. Similar to the situation for CO oxidation under dry condition, the formed carbonate species on MgO/Pt/Al<sub>2</sub>O<sub>3</sub> was quite stable even after Ar purge at 240 °C for 30 min. As discussed above, the stable and strongly adsorbed carbonate species could block the active Pt sites on MgO/Pt/Al<sub>2</sub>O<sub>3</sub> once the CO<sub>2</sub> was generated from CO oxidation, thus resulting in the low catalytic activity. Similarly, the poisoning of Pt sites by the *in situ* formed carbonate species in methanol decomposition would also lead to the low activity of MgO/Pt/Al<sub>2</sub>O<sub>3</sub> catalyst. In short summary, comparing to Pt/Al<sub>2</sub>O<sub>3</sub> and MgO/Pt/Al<sub>2</sub>O<sub>3</sub> catalysts, the abundant Ovac for methanol adsorption, rich Pt active sites with high Pt dispersion, as well as more acidic catalyst surface for high carbonate resistance simultaneously contributed to the superior methanol decomposition activity on WO<sub>3</sub>/Pt/Al<sub>2</sub>O<sub>3</sub> catalyst.

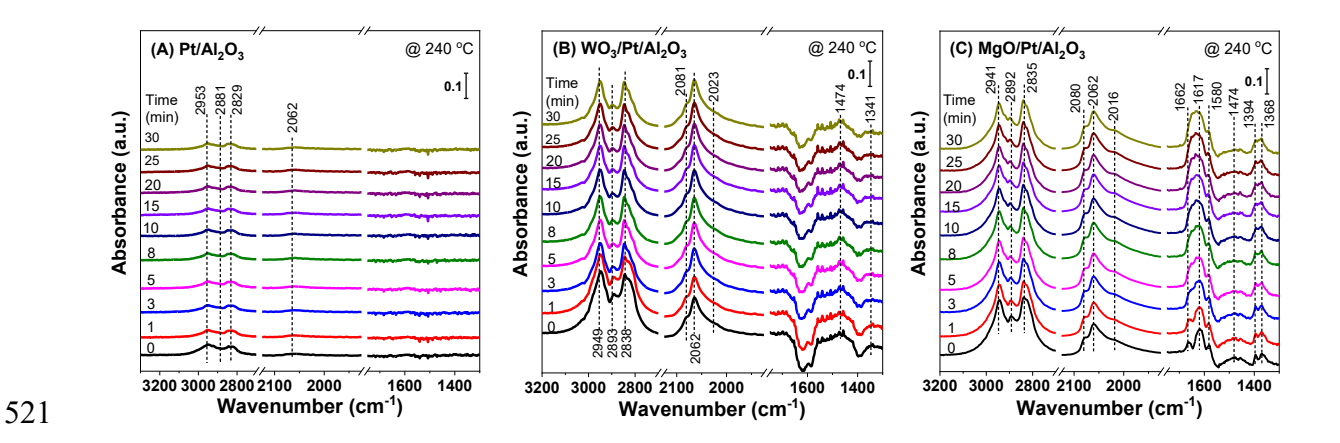


**Fig. 13.** *In situ* DRIFTS of methanol desorption at 240 °C for Pt/Al<sub>2</sub>O<sub>3</sub>, WO<sub>3</sub>/Pt/Al<sub>2</sub>O<sub>3</sub> and MgO/Pt/Al<sub>2</sub>O<sub>3</sub> catalysts.

#### 4. Conclusion

Pt/Al<sub>2</sub>O<sub>3</sub> single atom catalyst was successfully prepared using bayerite Al(OH)<sub>3</sub> as support through simple IWI method for Pt loading. With surface acidity modification on Pt/Al<sub>2</sub>O<sub>3</sub> by highly dispersed WO<sub>3</sub> and MgO, different catalytic behaviors were achieved on the catalysts in CO oxidation and methanol decomposition. Significant positive effect of H<sub>2</sub>O on CO oxidation was observed on the Pt/Al<sub>2</sub>O<sub>3</sub> based catalysts, particularly on the basic MgO modified MgO/Pt/Al<sub>2</sub>O<sub>3</sub> catalyst which performed the best CO oxidation activity under reaction condition with H<sub>2</sub>O. With acidic WO<sub>3</sub> modification, the WO<sub>3</sub>/Pt/Al<sub>2</sub>O<sub>3</sub> catalyst exhibited the best methanol decomposition activity among all the studied catalysts. By detailed *in situ* DRIFTS study, it was concluded that the positive H<sub>2</sub>O effect on CO oxidation activity was attributed to the inhibition of bicarbonate species formation on Pt/Al<sub>2</sub>O<sub>3</sub> and WO<sub>3</sub>/Pt/Al<sub>2</sub>O<sub>3</sub> catalysts and promoted carbonate desorption from MgO/Pt/Al<sub>2</sub>O<sub>3</sub>. The superior methanol decomposition activity on WO<sub>3</sub>/Pt/Al<sub>2</sub>O<sub>3</sub> was closely associated with its abundant oxygen vacancies and high resistance to carbonate accumulation.

#### 539 **Declaration of Competing Interest**

- 540 The authors declare that they have no known competing financial interests or personal
- relationships that could have appeared to influence the work reported in this paper.

# 542 Acknowledgement

- This work was supported by the Startup Fund from the University of Central Florida (UCF)
- and National Science Foundation grant (CHE-1955343). S. X. and X. Z. thank the support from
- 545 the Preeminent Postdoctoral Program (P3) at UCF. F. L. sincerely thanks Dr. Marcos
- 546 Schöneborn at Sasol for providing raw materials in catalyst synthesis. This research used
- 547 beamline 7-BM (QAS) of the National Synchrotron Light Source II, a U.S. Department of
- 548 Energy (DOE) Office of Science User Facility operated for the DOE Office of Science by
- Brookhaven National Laboratory under Contract No. DE-SC0012704.

#### 550 References

- 551 [1] Z. Li, S. Ji, Y. Liu, X. Cao, S. Tian, Y. Chen, Z. Niu, Y. Li, Well-defined materials for
- heterogeneous catalysis: From nanoparticles to isolated single-atom sites, Chem. Rev., 120
- 553 (2020) 623-682.
- 554 [2] L. Zhang, Y. Ren, W. Liu, A. Wang, T. Zhang, Single-atom catalyst: a rising star for green
- 555 synthesis of fine chemicals, Natl. Sci. Rev., 5 (2018) 653-672.
- 556 [3] A. Beniya, S. Higashi, Towards dense single-atom catalysts for future automotive
- 557 applications, Nat. Catal., 2 (2019) 590-602.
- 558 [4] X. He, Q. He, Y. Deng, M. Peng, H. Chen, Y. Zhang, S. Yao, M. Zhang, D. Xiao, D. Ma,
- B. Ge, H. Ji, A versatile route to fabricate single atom catalysts with high chemoselectivity and
- regioselectivity in hydrogenation, Nat. Commun., 10 (2019) 3663.
- 561 [5] Y. Nakaya, J. Hirayama, S. Yamazoe, K.I. Shimizu, S. Furukawa, Single-atom Pt in
- intermetallics as an ultrastable and selective catalyst for propane dehydrogenation, Nat.

- 563 Commun., 11 (2020) 2838.
- [6] K. Yang, Y. Liu, J. Deng, X. Zhao, J. Yang, Z. Han, Z. Hou, H. Dai, Three-dimensionally
- ordered mesoporous iron oxide-supported single-atom platinum: Highly active catalysts for
- benzene combustion, Appl. Catal. B: Environ., 244 (2019) 650-659.
- 567 [7] Z. Jiang, X. Feng, J. Deng, C. He, M. Douthwaite, Y. Yu, J. Liu, Z. Hao, Z. Zhao, Atomic-
- scale insights into the low-temperature oxidation of methanol over a single-atom Pt<sub>1</sub>-Co<sub>3</sub>O<sub>4</sub>
- 569 catalyst, Adv. Funct. Mater., 29 (2019) 1902041.
- 570 [8] M. Flytzani-Stephanopoulos, Supported metal catalysts at the single-atom limit A
- 571 viewpoint, Chin. J. Catal., 38 (2017) 1432-1442.
- 572 [9] N. Zhang, C. Ye, H. Yan, L. Li, H. He, D. Wang, Y. Li, Single-atom site catalysts for
- environmental catalysis, Nano Research, 13 (2020) 3165-3182.
- 574 [10] L.N. Chen, K.P. Hou, Y.S. Liu, Z.Y. Qi, Q. Zheng, Y.H. Lu, J.Y. Chen, J.L. Chen, C.W.
- Pao, S.B. Wang, Y.B. Li, S.H. Xie, F.D. Liu, D. Prendergast, L.E. Klebanoff, V. Stavila, M.D.
- 576 Allendorf, J. Guo, L.S. Zheng, J. Su, G.A. Somorjai, Efficient hydrogen production from
- methanol using a single-site Pt<sub>1</sub>/CeO<sub>2</sub> catalyst, J. Am. Chem. Soc., 141 (2019) 17995-17999.
- 578 [11] G. Xu, H. Wei, Y. Ren, J. Yin, A. Wang, T. Zhang, Chemoselective hydrogenation of 3-
- 579 nitrostyrene over a Pt/FeO<sub>x</sub> pseudo-single-atom-catalyst in CO<sub>2</sub>-expanded liquids, Green
- 580 Chemistry, 18 (2016) 1332-1338.
- [12] J. Jones, H. Xiong, A.T. DeLaRiva, E.J. Peterson, H. Pham, S.R. Challa, G. Qi, S. Oh,
- 582 M.H. Wiebenga, X.I.P. Hernández, Y. Wang, A.K. Datye, Thermally stable single-atom
- platinum-on-ceria catalysts via atom trapping, Science, 353 (2016) 150-154.
- 584 [13] L. Nie, D. Mei, H. Xiong, B. Peng, Z. Ren, X.I.P. Hernandez, A. DeLaRiva, M. Wang,
- M.H. Engelhard, L. Kovarik, Activation of surface lattice oxygen in single-atom Pt/CeO<sub>2</sub> for
- low-temperature CO oxidation, Science, 358 (2017) 1419-1423.
- 587 [14] S. Xie, W. Tan, C. Wang, H. Arandiyan, M. Garbrecht, L. Ma, S.N. Ehrlich, P. Xu, Y. Li,

- Y. Zhang, S. Collier, J. Deng, F. Liu, Structure-activity relationship of Pt catalyst on engineered
- 589 ceria-alumina support for CO oxidation, J. Catal., 405 (2022) 236-248.
- 590 [15] B. Qiao, A. Wang, X. Yang, L.F. Allard, Z. Jiang, Y. Cui, J. Liu, J. Li, T. Zhang, Single-
- atom catalysis of CO oxidation using Pt<sub>1</sub>/FeO<sub>x</sub>, Nat. Chem., 3 (2011) 634-641.
- 592 [16] W. Tan, H. Alsenani, S. Xie, Y. Cai, P. Xu, A. Liu, J. Ji, F. Gao, L. Dong, E. Chukwu, M.
- Yang, F. Liu, Tuning single-atom Pt<sub>1</sub>-CeO<sub>2</sub> catalyst for efficient CO and C<sub>3</sub>H<sub>6</sub> oxidation: Size
- effect of ceria on Pt structural evolution, ChemNanoMat, 6 (2020) 1797-1805.
- 595 [17] D. Yan, J. Chen, H. Jia, Temperature-induced structure reconstruction to prepare a
- thermally stable single-atom platinum catalyst, Angew. Chem. Int. Ed., 59 (2020) 13562-13567.
- 597 [18] Z. Qi, L. Chen, S. Zhang, J. Su, G.A. Somorjai, Mechanism of methanol decomposition
- over single-site Pt<sub>1</sub>/CeO<sub>2</sub> satalyst: A DRIFTS study, J. Am. Chem. Soc., 143 (2021) 60-64.
- 599 [19] S. Zhang, L. Chen, Z. Qi, L. Zhuo, J.L. Chen, C.W. Pao, J. Su, G.A. Somorjai, Insights
- into the mechanism of *n*-Hexane reforming over a single-site platinum catalyst, J. Am. Chem.
- 601 Soc., 142 (2020) 16533-16537.
- 602 [20] X. Ren, J. Li, S. Wang, D. Zhang, Y. Wang, Preparation and catalytic performance of
- ZrO2 supported Pt single-atom and cluster catalyst for hydrogenation of 2,4-dinitrotoluene to
- 604 2,4-toluenediamine, J. Chem. Technol. Biotechnol., 95 (2020) 1675-1682.
- [21] Z. Zhang, Y. Zhu, H. Asakura, B. Zhang, J. Zhang, M. Zhou, Y. Han, T. Tanaka, A. Wang,
- T. Zhang, N. Yan, Thermally stable single atom Pt/m-Al<sub>2</sub>O<sub>3</sub> for selective hydrogenation and
- 607 CO oxidation, Nat. Commun., 8 (2017) 16100.
- 608 [22] S. Liu, H. Xu, D. Liu, H. Yu, F. Zhang, P. Zhang, R. Zhang, W. Liu, Identify the activity
- origin of Pt single-atom catalyst via atom-by-atom counting, J. Am. Chem. Soc., 143 (2021)
- 610 15243-15249.
- [23] P. Christopher, Single-Atom Catalysts: Are All Sites Created Equal?, ACS Energy Lett.,
- 612 4 (2019) 2249-2250.

- 613 [24] J. Resasco, P. Christopher, Atomically dispersed Pt-group catalysts: Reactivity,
- uniformity, structural evolution, and paths to increased functionality, J. Phys. Chem. Lett., 11
- 615 (2020) 10114-10123.
- 616 [25] Y. Xu, M. Chu, F. Liu, X. Wang, Y. Liu, M. Cao, J. Gong, J. Luo, H. Lin, Y. Li, Q. Zhang,
- Revealing the correlation between catalytic selectivity and the local coordination environment
- of Pt single atom, Nano Lett., 20 (2020) 6865-6872.
- 619 [26] S. Zhao, J. Lin, P. Wu, C. Ye, Y. Li, A. Li, X. Jin, Y. Zhao, G. Chen, Y. Qiu, D. Ye, A
- 620 Hydrothermally stable single-atom catalyst of Pt supported on high-entropy oxide/Al<sub>2</sub>O<sub>3</sub>:
- Structural optimization and enhanced catalytic activity, ACS Appl. Mater. Interfaces, 13 (2021)
- 622 48764-48773.
- 623 [27] H. Wang, J. Dong, L.F. Allard, S. Lee, S. Oh, J. Wang, W. Li, M. Shen, M. Yang, Single-
- site Pt/La-Al<sub>2</sub>O<sub>3</sub> stabilized by barium as an active and stable catalyst in purifying CO and C<sub>3</sub>H<sub>6</sub>
- 625 emissions, Appl. Catal. B: Environ., 244 (2019) 327-339.
- 626 [28] R.C.R. Santos, A.N. Pinheiro, E.R. Leite, V.N. Freire, E. Longhinotti, A. Valentini,
- 627 Simple synthesis of Al<sub>2</sub>O<sub>3</sub> sphere composite from hybrid process with improved thermal
- stability for catalytic applications, Mater. Chem. Phys., 160 (2015) 119-130.
- [29] Karl Sohlberg, S.T. Pantelides, S.J. Pennycook, Surface reconstruction and the difference
- in surface acidity between  $\gamma$  and  $\eta$ -Alumina, J. Am. Chem. Soc., 123 (2001) 26-29.
- [30] L. Li, W. Han, F. Dong, L. Zong, Z. Tang, J. Zhang, Controlled pore size of ordered
- 632 mesoporous Al<sub>2</sub>O<sub>3</sub>-supported Mn/Cu catalysts for CO oxidation, Micro. Meso. Mater., 249
- 633 (2017) 1-9.
- 634 [31] J. Ke, W. Zhu, Y. Jiang, R. Si, Y.-J. Wang, S.-C. Li, C. Jin, H. Liu, W.-G. Song, C.-H.
- Yan, Y.-W. Zhang, Strong local coordination structure effects on subnanometer PtO<sub>x</sub> clusters
- over CeO<sub>2</sub> canowires probed by low-temperature CO oxidation, ACS Catal., 5 (2015) 5164-
- 637 5173.

- 638 [32] Y. Chen, Y. Feng, L. Li, J. Liu, X. Pan, W. Liu, F. Wei, Y. Cui, B. Qiao, X. Sun, X. Li, J.
- 639 Lin, S. Lin, X. Wang, T. Zhang, Identification of active sites on high-performance Pt/Al<sub>2</sub>O<sub>3</sub>
- catalyst for cryogenic CO oxidation, ACS Catal., 10 (2020) 8815-8824.
- [33] W. Tan, S. Xie, X. Wang, C. Wang, Y. Li, T.E. Shaw, L. Ma, S.N. Ehrlich, A. Liu, J. Ji,
- F. Gao, L. Dong, F. Liu, Highly efficient Pt catalyst on newly designed CeO<sub>2</sub>-ZrO<sub>2</sub>-Al<sub>2</sub>O<sub>3</sub>
- support for catalytic removal of pollutants from vehicle exhaust, Chem. Eng. J., 426 (2021)
- 644 131855.
- 645 [34] Seiji Yamazoe, Yutaka Hitomi, Tetsuya Shishido, T. Tanaka, XAFS study of tungsten L<sub>1</sub>-
- and L<sub>3</sub>-edges: Structural analysis of WO<sub>3</sub> species loaded on TiO<sub>2</sub> as a catalyst for photo-
- oxidation of NH<sub>3</sub>, J. Phys. Chem. C 112 (2008) 6869-6879.
- [35] H. Yue, P. Lu, W. Su, Y. Xing, R. Li, J. Wang, Simultaneous removal of NO<sub>x</sub> and Hg(0)
- from simulated flue gas over Cu<sub>a</sub>Ce<sub>b</sub>Zr<sub>c</sub>O<sub>3</sub>/r-Al<sub>2</sub>O<sub>3</sub> catalysts at low temperatures: performance,
- characterization, and mechanism, Environ. Sci. Pollut. Res. Int., 26 (2019) 13602-13618.
- [36] G. Yang, H. Zhao, X. Luo, K. Shi, H. Zhao, W. Wang, Q. Chen, H. Fan, T. Wu, Promotion
- effect and mechanism of the addition of Mo on the enhanced low temperature SCR of NO<sub>x</sub> by
- 653 NH<sub>3</sub> over MnO<sub>x</sub>/ $\gamma$ -Al<sub>2</sub>O<sub>3</sub> catalysts, Appl. Catal. B: Environ., 245 (2019) 743-752.
- 654 [37] H. Wang, R. Zhang, Y. Liu, P. Li, H. Chen, F.R. Wang, W.Y. Teoh, Selective catalytic
- oxidation of ammonia over nano Cu/zeolites with different topologies, Environ. Sci.: Nano, 7
- 656 (2020) 1399-1414.
- 657 [38] L. Yuan, X. Zheng, K. Duan, H. Hu, J. Wang, S.I. Woo, Z. Liu, The effect of preparation
- conditions of Pt/Al<sub>2</sub>O<sub>3</sub> on its catalytic performance for the H<sub>2</sub>-SCR in the presence of oxygen,
- 659 Front. Environ. Sci. Eng., 7 (2013) 457-463.
- 660 [39] I. Contreras-Andrade, A. Va'zquez-Zavala, T.s. Viveros, Influence of the synthesis
- method on the catalytic behavior of Pt and PtSn/Al<sub>2</sub>O<sub>3</sub> reforming catalyst, Energy Fuels 23
- 662 (2009) 3835–3841.

- 663 [40] G. Corro, J.L.G. Fierro, V.C. Odilon, An XPS evidence of Pt<sup>4+</sup> present on sulfated
- Pt/Al<sub>2</sub>O<sub>3</sub> and its effect on propane combustion, Catal. Comm., 4 (2003) 371-376.
- 665 [41] Q. Liu, H. Qin, J.A. Boscoboinik, G. Zhou, Comparative study of the oxidation of
- NiAl(100) by molecular oxygen and water vapor using ambient-pressure X-ray photoelectron
- spectroscopy, Langmuir, 32 (2016) 11414-11421.
- 668 [42] J. Raja, C.P.T. Nguyen, C. Lee, N. Balaji, S. Chatterjee, K. Jang, H. Kim, J. Yi, Improved
- data retention of InSnZnO nonvolatile memory by H<sub>2</sub>O<sub>2</sub> treated Al<sub>2</sub>O<sub>3</sub> tunneling layer: A cost-
- effective method, IEEE Electron Device Lett., 37 (2016) 1272-1275.
- 671 [43] C. Morterra;, A. Zecchina;, S. Coluccia;, A. Chiorin, I.r. spectroscopic study of CO
- adsorption onto  $\eta$ -Al<sub>2</sub>O<sub>3</sub>, J. Chem. Soc. Faraday Trans., 73 (1977) 1544-1560.
- 673 [44] D. Cornu, H. Guesmi, J.-M. Krafft, H. Lauron-Pernot, Lewis acido-basic interactions
- between CO<sub>2</sub> and MgO surface: DFT and DRIFT approaches, J. Phys. Chem. C, 116 (2012)
- 675 6645-6654.
- 676 [45] C. Wang, X.-K. Gu, H. Yan, Y. Lin, J. Li, D. Liu, W.-X. Li, J. Lu, Water-mediated Mars-
- Van Krevelen mechanism for CO oxidation on ceria-supported single-atom Pt<sub>1</sub> catalyst, ACS
- 678 Catal., 7 (2016) 887-891.
- [46] D. Teichmann, W. Arlt, P. Wasserscheid, R. Freymann, A future energy supply based on
- 680 Liquid Organic Hydrogen Carriers (LOHC), Energy Environ. Sci., 4 (2011) 2767.
- [47] C. Cao, K.L. Hohn, Study of reaction intermediates of methanol decomposition and
- catalytic partial oxidation on Pt/Al<sub>2</sub>O<sub>3</sub>, Appl. Catal. A: General, 354 (2009) 26-32.